

DOI: 10.17725/j.rensit.2024.16.173

Intelligent Metasurfaces, Fourier Optics and Cryptography: New Scientific Horizons

Alexander A. Potapov

Kotel'nikov Institute of Radioengineering and Electronics of RAS, <http://www.cplire.ru/>

Moscow 125009, Russian Federation

Jinan University, JNU-IREE RAS Joint Laboratory of Information Technology and Fractal Processing of Signals, <https://jnu.edu.cn/>

Guangzhou 510632, China

E-mail: potapov@cplire.ru

Received September 29, 2023, peer-reviewed October 02, 2023, accepted October 09, 2023, published April 25, 2024

Abstract: Reviews the current state of programmable and intelligent metasurfaces (MS) and their emerging applications in advanced integrated devices. For example, intelligent MS can adapt radio wave propagation channels and enhance their differences. The main strategies for designing intelligent MSs are considered. The necessity of combining such intelligent MSs with numerous methods of topological texture-fractal processing of signals and fields is revealed.

Keywords: photonics; radio photonics; nanotechnology; radiophysics; radar; radio engineering; texture; fractals; processing of multidimensional signals; frontier optics; computing metasurface; optical transfer function; optical analog computing

UDC 519.24+ 537.86+621.396.96

Acknowledgments: The research has been performed in the framework of the state task for IRE RAS, theme "Aether-2". The author expresses sincere gratitude to the Chinese scientists with whom articles on photonics were jointly completed and published in leading international scientific journals for the period 2019–2023: Weiping Liu, Tianhua Feng, Lei Wan, Danping Pan, Min Ouyang, Zixian Liang, Zhaohui Li, Shuaifeng Yang, Xia Wu, Yi Xu, Ning Lai, Weilian Chen, Fugen Wang, Jin Yuan, Xin Zhang, Wei Zhang, as well as all those scientists from China who promptly send me their recently published original works.

For citation: Alexander A. Potapov. Intelligent Metasurfaces, Fourier Optics and Cryptography: New Scientific Horizons. *RENSIT: Radioelectronics. Nanosystems. Information Technologies*, 2024, 16(2):173-206e. DOI: 10.17725/j.rensit.2024.16.173.

CONTENTS

- | | |
|--|---|
| <ol style="list-style-type: none"> 1. INTRODUCTION (174) 2. OPTICAL ANALOG COMPUTING BASED ON METASURFACES (175) 3. INTELLIGENT METASURFACES AND THEIR IMPORTANCE (176) <ol style="list-style-type: none"> 3.1. SMART METASURFACE PROPERTIES (176) 3.2. WIRELESS ARCHITECTURE WITH INTELLIGENT MS (177) 3.3. SMART SENSING WITH ALMOST NO DIGITAL COMPUTATION (177) 3.4. INTELLIGENT SENSING BASED ON HYBRID COMPUTING (178) | <ol style="list-style-type: none"> 3.5. INTELLIGENT INTEGRATED SENSING BASED ON HYBRID COMPUTING (178) 4. METASURFACES, DIGITAL CODING AND CRYPTOGRAPHY (178) 5. WIRELESS "MENTAL COMMUNICATION" THROUGH THE BRAIN-COMPUTER-MS PLATFORM (181) <ol style="list-style-type: none"> 5.1. ELECTROMAGNETIC BRAIN-COMPUTER-MS PLATFORM FOR NON-INVASIVE CONTROL OF INFORMATION SYNTHESIS AND ITS WIRELESS TRANSMISSION (181) 5.2. WIRELESS "MENTAL COMMUNICATION" BETWEEN TWO OPERATORS (183) |
|--|---|

- 5.3. IMPLEMENTATION OF THE EXPERIMENT AND RESULTS OF WIRELESS COMMUNICATION (184)
- 5.4. WAVEFRONT SYNTHESIS USING EBCM (185)
- 5.5. TOWARDS NEW GENERATIONS OF BIOINTELLIGENT METASURFACE SYSTEMS (187)
6. PROGRAMMABLE MS FOR WIRELESS ENCRYPTION (187)
- 6.1. A SHORT INTRODUCTION (187)
- 6.2. WIRELESS COMMUNICATION ENCRYPTION SCHEME BASED ON PROGRAMMABLE POLARIZATION-MODULATED INFORMATION MS (188)
- 6.3. SIMULATION RESULTS (189)
- 6.4. MEASUREMENT RESULTS (191)
- 6.5. METAKEY BASED ON MP PoM (193)
- 6.6. IMPLEMENTATION OF A WIRELESS COMMUNICATION SYSTEM WITH PoM ENCRYPTION (193)
- 6.7. DECODING FEATURES (195)
7. OPTICAL ENCRYPTION AT SPATIAL FREQUENCIES USING MS (197)
- 7.1. INTRODUCTORY PART (197)
- 7.2. WORKING PRINCIPLES (197)
- 7.3. SIGNAL INTENSITY ENCRYPTION IN THE SPATIAL FREQUENCY DOMAIN (198)
- 7.4. PHASE ENCRYPTION AT SPATIAL FREQUENCY (200)
- 7.5. SPATIAL FREQUENCY MULTIPLEXING TO INCREASE ENCRYPTION CAPACITY (201)
- 7.6. FEATURES AND PROSPECTS OF ENCRYPTION AT SPATIAL FREQUENCIES (202)
8. CONCLUSION (203)
- REFERENCES(203)

1. INTRODUCTION

In recent years, promising applications of artificial intelligence (AI) have emerged in many disciplines, including optics, engineering,

medicine, economics, etc. In particular, the synergy between AI and meta-optics brings great benefits to both fields. Meta-optics are advanced flat optics with new functions and light control capabilities [1]. Metamaterials enable precise tailoring of light-matter interactions at subwavelength scales, providing access to the full range of electromagnetic reactions encoded in Maxwell's equations and operating across a huge swath of the electromagnetic spectrum. Metasurfaces (MS) are planar subwavelength optical devices that can manipulate light (electromagnetic waves). The MS consists of a specially located array of meta-atoms. Artificial meta-atoms are designed and calculated to control the phase, amplitude and polarization of incident electromagnetic waves. The new wavefront can be reconstructed by the MS. Numerous functions of meta-devices can be realized through several steps such as material selection, meta-atom design, phase distribution design, layout configuration, fabrication, characterization, and application demonstration. These steps have been presented in detail in previous reviews [2–8].

In **Fig. 1** shows the development trend of AI (red) and meta-optics (blue) [1]. Coincidentally, both areas began to grow rapidly around 2012. A detailed explanation of the main stages of the development of AI

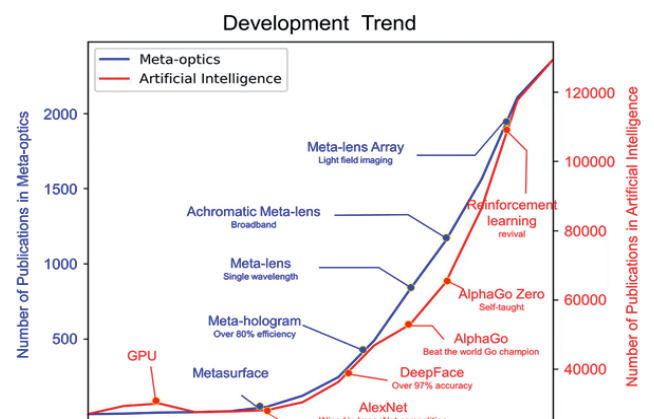


Fig. 1. Trends in the development of AI and meta-optics (the number of publications per year was collected from a search in the Web of Science [1]).

and meta-optics in Fig. 1 is given in [1]. Mainly, the review [1] classifies and discusses recent developments integrated under two themes, namely AI for meta-optics and meta-optics for AI. The first describes how to apply AI to meta-optics research for design, simulation, optical information analysis and application. The second reports on the development of optical systems and calculations using metaoptics.

This work is a direct continuation of the author’s previous review on the physics and design of basic computational dielectric MSs and their applications [9], which takes into account research with Chinese scientists in the joint laboratory of information technology and fractal signal processing in China for the period 2022-2023. [10-17].

2. OPTICAL ANALOG COMPUTING BASED ON METASURPHACES

In the face of increasingly complex information technologies, the question of how to improve processing performance, operating speed, and efficient computing capabilities has become an important issue in the information and engineering fields. Compared with traditional analog computing, optical analog operation is realized through light modulation. Thus, this process is parallel and passive, and its advantages are low power consumption and high operating speed. A historical overview of optical analog computing is given in review

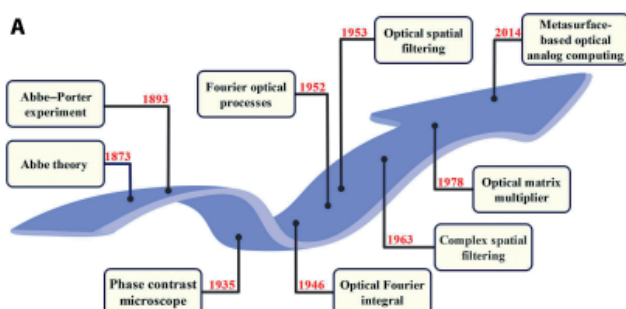


Fig. 2. Development of optical analog computing [18].

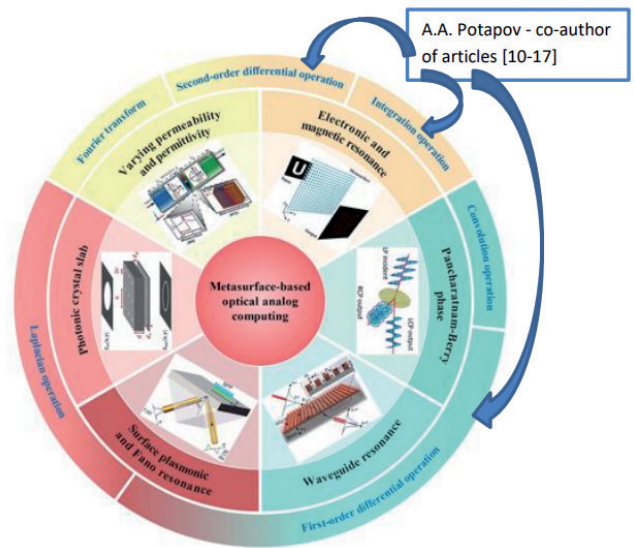


Fig. 3. Various physical bases of optical analog operations [18] (adapted).

[18] and shown in Fig. 2, and their physics – in a pie chart (Fig. 3, with additions).

As the most intuitive method for object perception, image edge detection is an integral part of image recognition, AI, and machine learning [10–18]. Image edge detection can simply be viewed as a high-pass filtering process that enhances useful high spatial frequency information and suppresses irrelevant low spatial frequency information. Optical analog computing has received a lot of attention recently. Additionally, optical analog computing has also demonstrated unique potential in convolution performance and solving complex mathematical equations. Their high integration, high response speed, and precise control of optical analog operations make them a promising tool for specific multidimensional signal processing applications.

The function of the MS is to manipulate the wavefront of incident light by adapting the phase profile of a given operating wavelength. The method of achieving full 2π phase modulation is the key to achieving complete wavefront control. Dielectric

metaatoms support various local resonances of strong electric and magnetic scattering, which are described using Mie theory. When the frequency of the incident light is below or near the bandgap frequency of the dielectric material, the electric dipole and magnetic dipole resonances are excited. A dielectric Mie resonator includes various electrical and magnetic components that allow the creation of electromagnetic waves [1].

When certain resonances are excited in the MS by electromagnetic waves, abrupt phase changes can be observed. These resonances can be divided into electrical resonance and magnetic resonance depending on the dipole moment of the corresponding structure. The simplest class of MSs consists of subwavelength periodic arrays of dielectric or metallic inclusions that have a purely electric dipole response, while Huygens MSs include an electrical response and a magnetic response [10,12,15,18]. Huygens surface is an MS used to achieve a specific wavefront using the Huygens principle. The overall response of the MS is governed by Huygens' principle, where each point on the wave front is a source of secondary waves. Modulation of electric and magnetic dipoles on the Huygens MS can control the stray field. In particular, [19] demonstrates a path to high-quality factorial wavefront generation in two spatial dimensions based on all-dielectric Huygens MSs using higher order Mie resonances in the near-IR region.

3. INTELLIGENT METASURFACES AND THEIR IMPORTANCE

3.1. SMART METASURFACES PROPERTIES

The simultaneous control of electromagnetic waves and information using information MSs is of central importance in the modern world. Metamaterials have evolved from engineered structures to intelligent wave agents and have achieved enormous success in controlling

the interaction of wave, information and matter, which could not be achieved with natural materials [20]. Recently, conventional structural or passive MSs have made a significant step forward towards intelligent MSs through integration with algorithms and nonlinear materials or active devices [1,6,20-23]. The smart MS metaatom is integrated with tunable functional materials or active devices and is designed for in-situ reprogramming under the control of appropriate algorithms. Unlike conventional MS, intelligent MS has three important properties: digitalization, programmability and intelligence, giving us the ability to control the interaction of wave, information and matter without human intervention. Here, digitalization allows the intelligent MS to encode/decode and store digital information at the physical level. Programmability means that an intelligent MS is capable of implementing various functions with one physical entity, and switching between them by changing control code sequences. While intelligence indicates that an intelligent MS has local or cloud algorithms as its brain and is capable of making decisions, self-programming and performing a series of sequential tasks without human control [20]. Therefore, reconfigurable and reprogrammable MSs can be classified as the infancy stage of intelligent MS, since they are not strictly intelligent according to the above definition.

In short, intelligent MSs can provide us with intelligent platforms for manipulating wave-information interactions of matter, which have promising potentials in establishing a direct connection between the physical world and the digital world and serve the natural role of merging the physical entity with its digital counterpart. Intelligence is the core of intelligent MSs, and algorithms (especially deep learning methods) can fill this role well.

Historically, two important developments have occurred during the evolution of intelligent MSs: active MSs and programmable MS encodings. Unlike passive (i.e. structural only) MSs, active MSs are hybrid structures, embedded tunable functional materials (for example, chalcogenide compound $\text{Ge}_2\text{Sb}_2\text{Te}_3$) and active elements (PIN diodes, varactors and MEMS switches), allowing us to dynamically manage the wave-information-matter interaction due to energy consumption. In programmable MSs, each meta-atom being built has a finite number of quantized physical states and can be used to encode digital information at the physical level, connecting the digital world and the physical world. An intelligent MS consists of controllable meta-atoms, and each meta-atom has a number of quantized physical states.

Most of the modern options for designing a smart MS, methods for converting a beam of illumination incident on a MS into a beam with the desired wavefront and/or waveform, wireless energy transfer and energy harvesting in the Internet of Things (IoT) society, and methods for generating dynamic holograms using smart MSs are given in [20,23].

3.2. WIRELESS ARCHITECTURE WITH INTELLIGENT MS

Wireless communication has become an important tool for addressing the ever-increasing needs for wireless information transmission in modern society. Basic smart MS wireless communication architectures (or reconfigurable smart surface) have been proposed recently and are classified into three main types in [20]: (A) non-modulated metasurface backscatter communications (NMMBC), (B) modulated metasurface backscatter (NMMBC). MMCC) and (C) ambient modulated metasurface backscatter communications (AMMBC)

3.3. SMART SENSING WITH ALMOST NO DIGITAL COMPUTATION

Smart sensing with almost no digital computation is presented in [20]. Currently, for most practical sensor systems, the most important but challenging problem is dealing with high-dimensional data or "data crisis". Fortunately, multidimensional data has some structured representations in many practical scenarios. The famous Johnson-Lindenstrauss Lemma states that structured high-dimensional data can be projected into low-dimensional feature space with almost negligible information loss through a properly designed linear transformation [24]. In other words, significant information about multidimensional data can be obtained from its surprisingly reduced dimensions under most practical conditions. To date, there are many popular linear embedding transformations with the so-called restricted isometry property. Among them, some embedding transformations, such as principle component analysis (PCA), allow the creation of low-dimensional representations with mathematically or physically meaningful features, implying that target information can be well extracted from these low-dimensional features with almost no digital computation.

The use of linear embedding methods in smart metasurface sensors is considered in [25]. Intelligent MS is capable of generating almost arbitrary radiation patterns or measurement modes using machine learning methods. The concept of a machine learning reprogrammable thermal imager has been proposed [25], in which an intelligent MS is trained with a huge amount of training data using PCA, so that the radiation patterns desired by the machine learning can be achieved at the physical level. The smart MS then serves as a physical computing device that infers low-dimensional PCA functions from high-dimensional raw data inputs in an analog computational manner.

Thus, the resulting sensing strategy is almost free of digital computation. The smart MS is designed to operate at a frequency of about 3 GHz. It can be concluded that the machine learning sensing strategy can obtain high-quality real-time images with almost ignorable digital computation, and such a sensing strategy will provide us with a promising route for intelligent sensing at different frequencies and beyond.

3.4. INTELLIGENT SENSING BASED ON HYBRID COMPUTING

Recently, the use of wireless signals in sensing, especially human behavior sensing, has gained intense attraction among researchers, but these strategies suffer from limited spatiotemporal image resolution and recognition accuracy due to the limited size of the field of view. In contrast to these methods, the three-pronged critical roles of intelligent MS should be highlighted here [20]. First, intelligent MS is used to sensing people in real time in a full view scene with high temporal-spatial resolution. Secondly, intelligent MS manipulates electromagnetic wave fields (such as ambient wireless signals) towards local points of interest to effectively recognize fine-grained body features, through which unwanted interference from the environment and other body parts can be significantly suppressed. Finally, body cues (such as subtle body language) and the physiological state of multiple non-contacting individuals can be clearly identified in real time.

3.5. INTELLIGENT INTEGRATED SENSING BASED ON HYBRID COMPUTING

To take full advantage of intelligence across the entire sensing chain, the three building blocks of intelligent sensing—the scene in the physical world, the data in the digital world, and the measure connecting the two worlds—must be considered together in a unique learning pipeline [20].

Intelligent MS deployed in physical environments has a very strong electromagnetic coupling with the environment and targets. However, to date, the environment has been largely treated as free space, such as in the field of wireless communications, which is obviously unrealistic and has a significant negative impact on the performance of information collection and processing. Therefore, it is necessary to model realistic interactions between intelligent MSs and the environment. Intelligent MS can adapt distribution channels and enhance their differences.

4. METASURFACES, DIGITAL CODING AND CRYPTOGRAPHY

Information security is an important topic, it always occupies a significant place in the daily life of modern society and thus gives rise to various modern encryption methods. Several interesting works on holographic encryption based on MP technology have been reported [26–28], which have demonstrated great potential value in optical encryption systems. By modulating both spectral and polarization responses, metasurface holography has been successfully applied to hide different information in different colors and polarization channels.

Optical encryption uses abundant degrees of freedom of light (such as amplitude, phase, polarization, wavelength, orbital angular momentum and dynamic control, as well as combinations thereof) to encode and decode target information, opening up new possibilities for information transmission and storage. A recently published paper [29] proposes a digital programmable MT with element-independent visible light sensing; The MP can be adaptively reprogrammed to achieve different electromagnetic functions by sensing color changes in incident light. This MP is integrated with three-color color sensors

(TCS3200), microcontrollers and a preload coding algorithm. By establishing feedback with a field programmable gate array (FPGA), the MP forms a complete intelligent adaptive and reconfigurable encoding system. The MP consists of 16x16 meta-cells, with four meta-atoms per group, each group integrating a trichromatic sensor and a chip.

The algorithm links the process of photosensitive MSs from detection to sensor data, data comparison, and finally the formation of different voltage distribution models on the MS. Specifically, when light frequency information is sensed by the trichromatic sensors and output to the high-speed ADC, it determines whether a threshold has been exceeded, and then the FPGA determines the threshold decision and drives the PIN diode on the MS to perform color encoding that matches the current threshold. For example, when the FPGA detects that the incident light is red, the MS performs dual beam encoding; when the incident light is green, the MS performs four-beam encoding; and when the incident light

is blue, the MT performs radar cross-section (RCS) coding.

In [29] a description of the created metasurface architecture for electromagnetic field modulation is given – **Fig. 4**. The metacell has three layers. The first layer is a metal patch with a thickness of 0.1 mm, the middle layer is a FR-4 layer with $\epsilon = 4.3$ and $\tan\delta = 0.025$, and the bottom layer is a metal screen. To achieve dynamic tuning of the device, a PIN diode (Skyworks SMP1320) is installed between two symmetrical metal patches in the first layer. In addition, to connect the control circuit, the block has two through holes with a diameter of 0.15 mm. In the process of simulation verification using the CST Microwave Studio microwave structure modeling system, a model of a metamaterial block (shown in Fig. 4a) with a period $p = 14$ mm and a medium thickness $b = 3.5$ mm was established. Other parameters: $a = 12$ mm, $w = 3$ mm, $w_1 = 4.5$ mm, $l = 1.7$ mm and $l_1 = 4.5$ mm.

The equivalent circuits of a PIN diode based on the R-L-C model are shown in Fig. 4b. The code "0" indicates that the PIN diode is in the "OFF" state, with $R1 = 0$, $L1 = 0.4$ nH and $C1 = 0.4$ pF. The code "1" indicates that the PIN diode is in the "ON" state, where $R2 = 2.2$, $L2 = 0.4$ nH and $C2 = 0$ pF. The amplitude and phase curves of the metamaterial element with y-polarization are shown in Fig. 4c,d. At the frequency point of 4.1 GHz, the phase difference between the two states of the element is π , and the amplitudes of the two states are -0.27 dB and -0.99 dB, respectively, showing that the metasurface wavefront is well controlled. Returning to the history of the issue, it should be especially noted that in 2014 one of the first works on digital coding of programmable metamaterials/metasurfaces was published [30], which integrates digital information into the design of metamaterials, connecting the physical worlds and the worlds of digital coding.

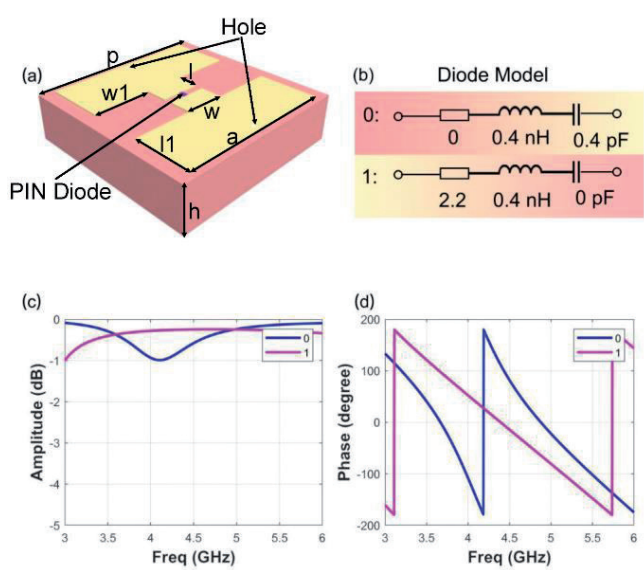


Fig. 4. Description of the structure and EM response of a meta-atom [29]: a) Three-dimensional view of a supercell. b) Equivalent circuit of PIN diode in OFF/ON state. c) amplitude response of the element. d) phase response of the element.

Returning to the history of the issue, it should be especially noted that in 2014 one of the first works on digital coding of programmable metamaterials/metasurfaces was published [30], which integrates digital information into the design of metamaterials, connecting the physical worlds and the worlds of digital coding. All results in paper [30] are based on the concept of metamaterial coding. Let's start with 1-bit MP encoding – Fig. 5a. We consider a special MP, which consists of binary digital elements '0' or '1'. In the binary case, the maximum phase difference is π (or 180°). Therefore, we design element "0" as a metamaterial particle with a 0-phase response, and element "1" as a metamaterial particle with a π phase response. Thus, the phase responses of elements '0' and '1' are simply defined as $\varphi_n = n\pi$ ($n = 0.1$). To achieve wide frequency bandwidth, a subwavelength square metal patch insert printed on a dielectric substrate is used to implement the binary elements (see inset Fig. 5b).

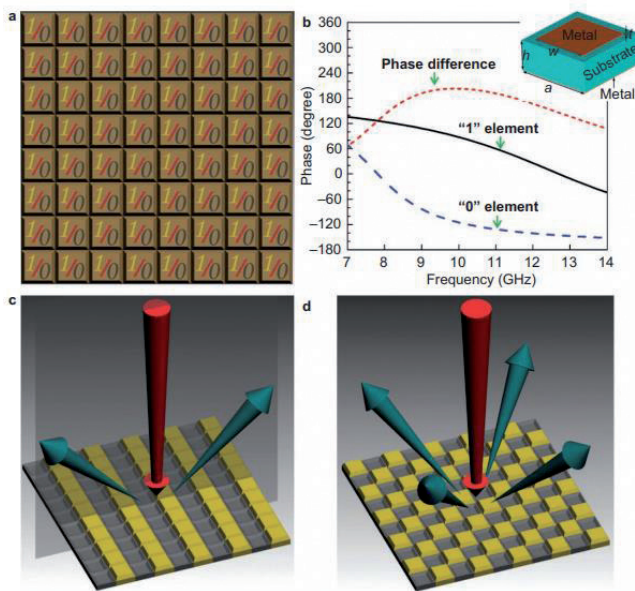


Fig. 5. 1-bit digital MP and MP coding [30]: (a) 1-bit digital MP consists of only two types of elements: '0' and '1'. (b) square metal patch block structure (insert) to implement elements "0" and "1" and the corresponding phase characteristics in the frequency range. (c) Two 1-bit periodic encoding MPs to control beam scattering by designing '0' and '1' element encoding sequences: (c) 010101.../010101... code and (d) 010101.../101010... code.

Unlike existing analog metamaterials, which use effective media parameters or special dispersion relations to control electromagnetic fields, encoding metamaterials simply manipulate electromagnetic waves through various encoding sequences of "0" and "1" elements. For example, with a periodic coding sequence 010101.../010101..., a normally incident beam will be mainly reflected by the MF in two symmetrically oriented directions, whereas with a periodic coding sequence 010101.../101010.../010101.../101010..., usually the incident beam will be mainly reflected in four symmetrically oriented directions, as shown in Fig. 5c and 5d.

The concept of encoding metamaterial can be extended from 1-bit encoding to 2-bit encoding or higher [30]. In 2-bit encoding, four types of unit cells with different responses should simulate the elements '00', '01', '10' and '11'. 2-bit encoding has greater freedom to manipulate electromagnetic waves than 1-bit encoding, but requires more sophisticated technology to digitally control. Similar to the 1-bit case, the four types of unit cells in 2-bit encoding metamaterials should have phase responses of 0 , $\pi/2$, π and $3\pi/2$, corresponding to the elements '00', '01', '10'

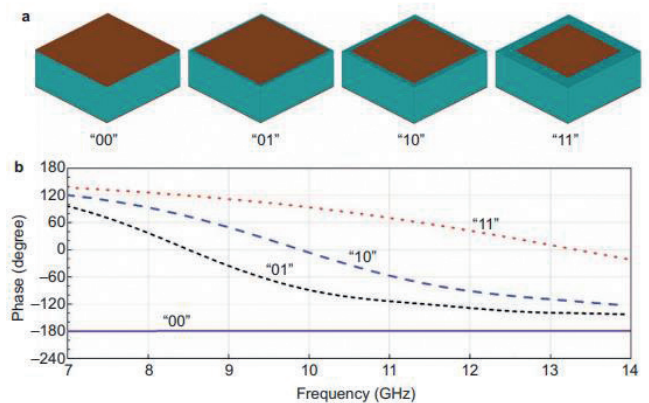


Fig. 6. 2-bit encoding of metasurface elements and their phase responses [30]: (a) elements "00", "01", "10" and "11" (from left to right), made using square metal patch blocks of various sizes. (b) phase responses of elements "00", "01", "10" and "11".

and '11' respectively. Therefore, the phase responses φ_n are simply defined as $\varphi_n = n\pi/2$, ($n = 0,1,2,3$).

To realize these metamaterial particles, [30] still uses square metal patch inserts of various sizes printed on a dielectric substrate to design elements "00", "01", "10" and "11", as shown in **Fig. 6**. With 2-bit metamaterial or MS encoding, we have greater flexibility in controlling encoding sequences to achieve broader applications. Proposed encoding metamaterials, digital metamaterials and programmable metamaterials, as noted in [30], are very attractive for various applications such as beam steering of antennas (similar to phase array antennas, but using a different principle with a much less expensive approach), performance reduction scattering targets and implementing other intelligent metamaterials. Next, we will consider the most typical examples of intelligent MPs. Let's start with a unique example of intelligent MT, published in June 2022 [31].

5. WIRELESS "MENTAL COMMUNICATION" THROUGH THE BRAIN-COMPUTER-MS PLATFORM

The study of the mechanisms of the human brain, and, in particular, the study of the mechanisms that support mental processes, is one of the pressing problems of modern science. Chinese scientists have introduced an electromagnetic brain-computer interface (BCI) smart MS controlled by brain signals directly and non-invasively [31]. In their work, scientists developed and experimentally confirmed the possibility of wireless "mental communication" and remote control of the "power of thought." The device uses non-invasive electrodes that read the electroencephalogram (EEG) using the

evoked potential method at the P300 wave. Let me remind you that the P300 wave (P3) is an event-related potential component that arises in the decision-making process. It is believed that this is an endogenous (originating from a living system) potential, since its occurrence is associated not with the physical properties of the stimulus, but with the person's reaction to it. It is claimed that brain activity can be turned into radio waves using programmable MS. This technology paves the way for mind-controlled radar, tired driver detection systems, and other applications.

5.1. ELECTROMAGNETIC BRAIN-COMPUTER-MS PLATFORM FOR NON-INVASIVE CONTROL OF INFORMATION SYNTHESIS AND ITS WIRELESS TRANSMISSION

Recently, reprogrammable MSs, including PIN diodes, varicaps, and micro/nanoelectromechanical systems (MEMS/NEMS) [21,23], have enabled real-time active and programmable control of electromagnetic field functions that were previously static or completely limited in conventional passive counterparts. In [31], an electromagnetic brain-computer-CM (EBCM) platform was first proposed and created for non-invasive control of information synthesis and its wireless transmission – **Fig. 7**. An operator equipped with electrodes and a P300 BCI device can directly control the MS with various electromagnetic functions under visual stimulus using specific timing encoding sequences. In **Fig. 7a** shows four typical circuits, including wireless brain communication, coding pattern decoding, beam scanning, and electromagnetic modulation multifunctionality.

The display is placed in front of the operator to display a graphical user interface (GUI) and has a virtual matrix of buttons, as shown in **Fig. 7b**. Different buttons correspond to different operations of the EBCM encoding pattern. Each attempt corresponds to one

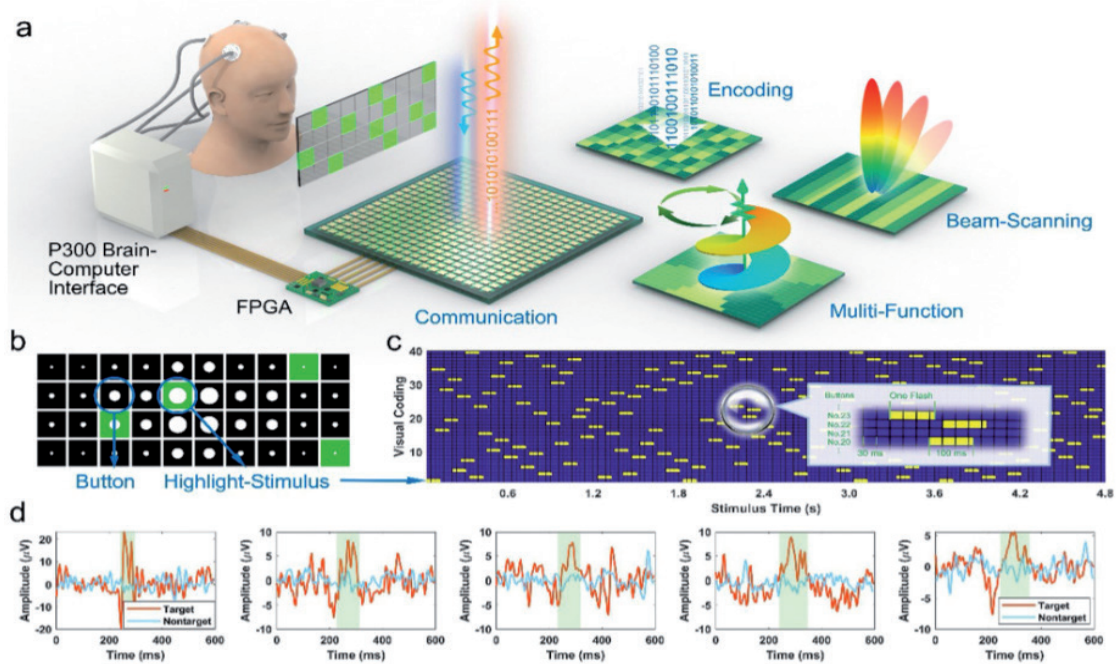


Fig. 7. EBCM platform [31]: (a) EBCM system architecture. (b) Graphical user interface of the beam deflection circuit. Buttons with different circles represent different directions of beam scattering, where the highlighted stimulus is green blocks. (c) Schematic diagram of a stimulus sequence in which 40 lines represent 40 buttons and yellow blocks mark button highlighting, each lasting 100 ms. (d) Experimentally measured EEG signals of five button presses, where obvious amplitude peaks occur at approximately 300 ms.

command being sent, and the buttons begin to flash sequentially in a random order for about 5 rounds, each containing one flash for each button. The flash sequence is randomly generated before each trial. Fig. 7c shows the flashing sequence of 40 buttons (40 rows) in a beam scanning pattern, where the yellow squares indicate the stimulus starting point.

The vertical axis represents the number of buttons from 1 to 40, and the horizontal axis represents 160 consecutive stimulus flashes, indicated by yellow bars in Fig. 7c. Each marked block in Fig. 7c corresponds to a duration of 30ms, and each flash lasts 100 ms, which covers just over 3 blocks. In Fig. 7c, we additionally show an enlarged image of the three flashes to more clearly illustrate the temporal sequences of the different button stimuli.

The operator's attention is focused on the button corresponding to the command he would like to issue (i.e., the target). When the target flashes, a positive potential can be

detected on the EEG after approximately 300 ms, called the P30034 potential. Such a P300-based BCI has been experimentally proven to be effective for direct brain control of external devices. To represent the brain signals for two types of stimuli (target and non-target), Fig. 7d shows the measured EEG signals, where the red and blue curves correspond to the signals for the target and non-target stimulus, respectively. In each sub-figure Fig. 7d signals corresponding to both the target and non-target buttons are averaged over multiple flashes. For each button flash in a trial, the EEG signal segment from 0 to 600 ms after flash onset is extracted and corrected using the baseline extracted from 200 ms before flash onset. This serial stimulus is then used to directly control a programmable logic integrated circuit (FPGA) to execute the appropriate instructions.

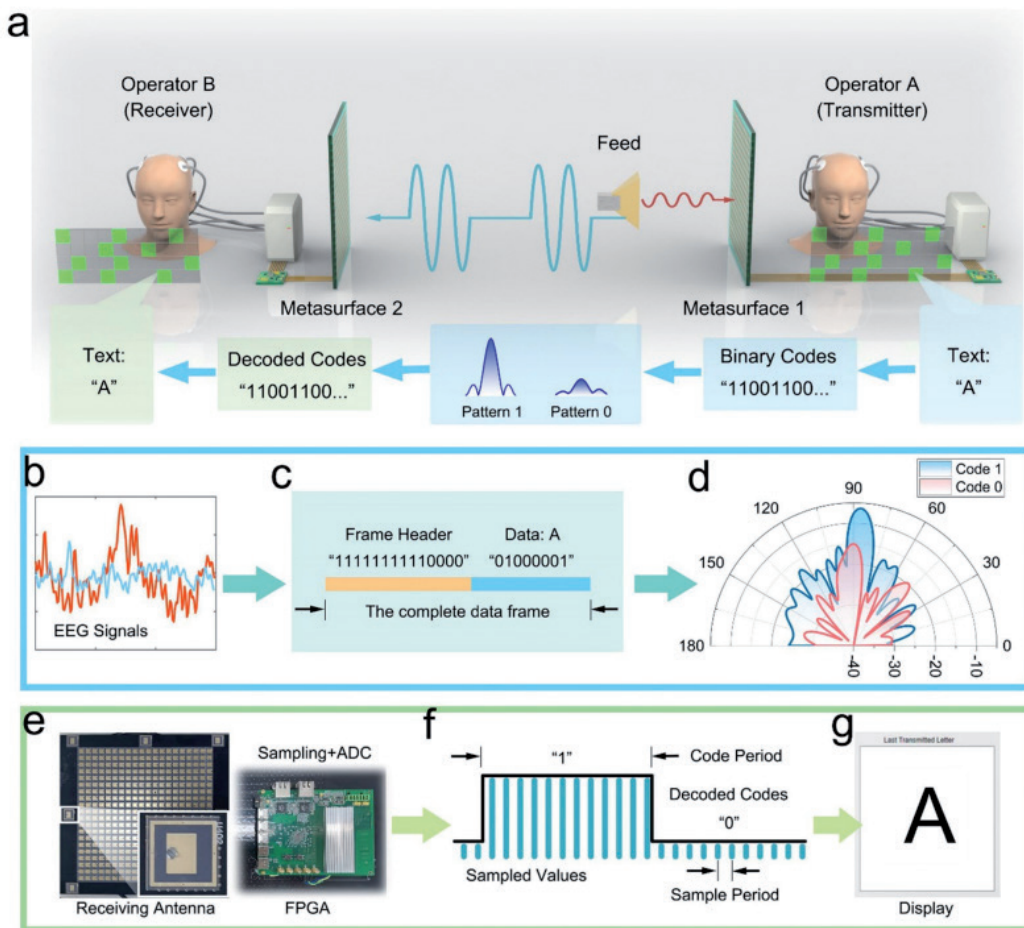


Fig. 8. *Wireless text communication using EBCM [31]: a) system architecture of the text messaging system and the encoding and decoding process. (b)-(d) The process of encoding EEG signals into transmitted electromagnetic signals, where the EEG signals shown in (b) are first detected by the BCI and converted into a digital sequence (c) for wireless transmission, and then emitted by MT with different amplitudes (d). (e)-(g) Wireless decoding process where the antenna and FPGA (e) first receive and sample signals from space and convert them into digital signals. The sample data is sampled into 0/1 codes for decoding (f), and finally translated into text for display (g).*

5.2. WIRELESS "MENTAL COMMUNICATION" BETWEEN TWO OPERATORS

As a demonstration of the EBCM concept, [31] presents a wireless "mental communication" between two operators – **Fig. 8a**. The BCI operator is provided with a text-based graphical interface in which the visual button is encoded directly as a specific encoding sequence consisting of "0" and "1" associated with two encoding patterns. Uses a high gain single beam pattern and a scatter reduction pattern for amplitude modulation, respectively "1" (high amplitude) and "0" (low amplitude). The prototype proof shows the wireless transmission of text mentally from

one operator to another within an EBCM communication system. Operator A, as a text transmitter, sends letters by visually looking at the character button in the EBCM GUI. When the target letter is decoded from the EEG signals, an encoding sequence based on ASCII codes is implemented on the FPGA to switch time-varying patterns.

During the encoding process, since buttons representing associated text characters have corresponding ASCII codes, the selected button is directly converted into binary ASCII codes with the frame header "11111111110000", as shown in Fig. 8c. Then, according to the final code, the MP reflects high or low intensity in

space. In the decoding process, we first collect spatial electromagnetic energy using a receiving channel including a microstrip antenna built near the MP, as shown in Fig. 8e, as well as a low noise amplifier (LNA) and a high-speed analog-to-digital converter (ADC) controlled by an FPGA. The collected data stream is a set of consecutive frames that represents the measured intensity at a data acquisition rate of 10 MHz. A decoding algorithm is used to determine the position of the frame header to determine the starting point of the data frame, as shown in Fig. 8f. The sample data is then converted into ASCII binary codes and the text is then displayed in a GUI.

Four text sequences are successfully sent and received using the EBCM platform, including “HELLO WORLD”, “HI, SEU”, “HI, SCUT” and “BCI METASURFACE”. The average time to enter each character is about 5 seconds. when using a P300 based BCI by an experienced BCI operator. Since a programmable MP can achieve a 0/1 code rate of at least 1 Mbit/s, the maximum symbol rate for an MS is about $5 \cdot 10^4$ symbols per second (20 bits per sequence). Therefore, the final text transmission rate is about 12 characters per minute. It is worth noting that P300-based BCIs provide greater accuracy and reliability among various non-invasive BCIs.

5.3. IMPLEMENTATION OF THE EXPERIMENT AND RESULTS OF WIRELESS COMMUNICATION

The communication system is shown in detail in Fig. 9a [31]. In the transmission part, EEG signals are first detected and processed by BCI devices and translated into corresponding FPGA control signals. The control signals follow the coding principle of the corresponding interface signals shown in Fig. 7b-7d.

The FPGA performs the encoding and switches the PIN diodes to the required

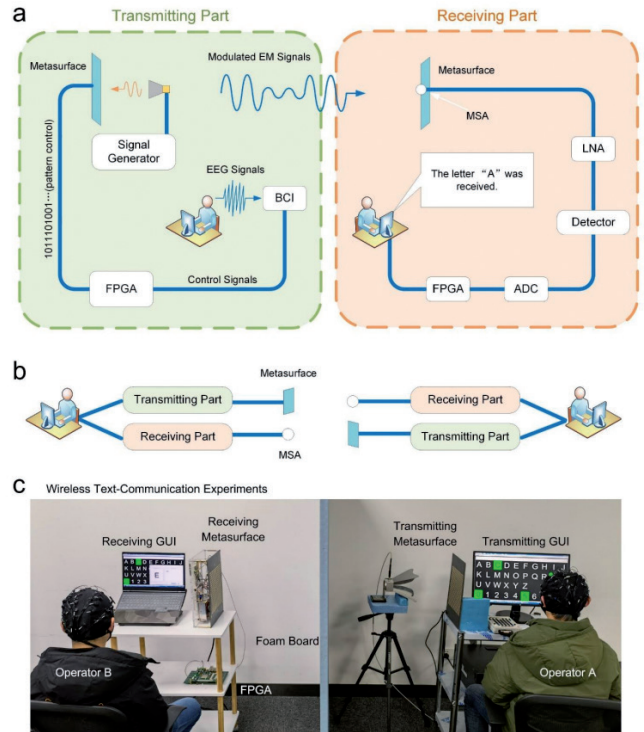


Fig. 9. Experimental implementation of wireless text communication [31]: (a) System architecture of the wireless text communication experiment. (b) Illustration of the working mechanism of the transmitting and receiving parts. (c) Experimental scenario of wireless text communication directly over EBCM, where a foam panel is placed between two operators to test the wireless communication properties.

states. In the receiving part, a microstrip antenna (MSA) near the metasurface receives electromagnetic signals from the transmitter and forwards them to the LNA and detector. The detector samples analog amplitude, which is then converted into digital codes for the FPGA. The presented process is unidirectional, but the EBCM communication system is bidirectional because the transmit and receive fronts are metasurface and MPA respectively, as shown in Fig. 9b.

The experimental scenario is presented in Fig. 9c, in which Operator A performs the task of transmitting text and Operator B receives and reads the text. The distance between the transmitting and receiving MF is about 1.3 m, while the transmitting MF is excited by a broadband antenna from a

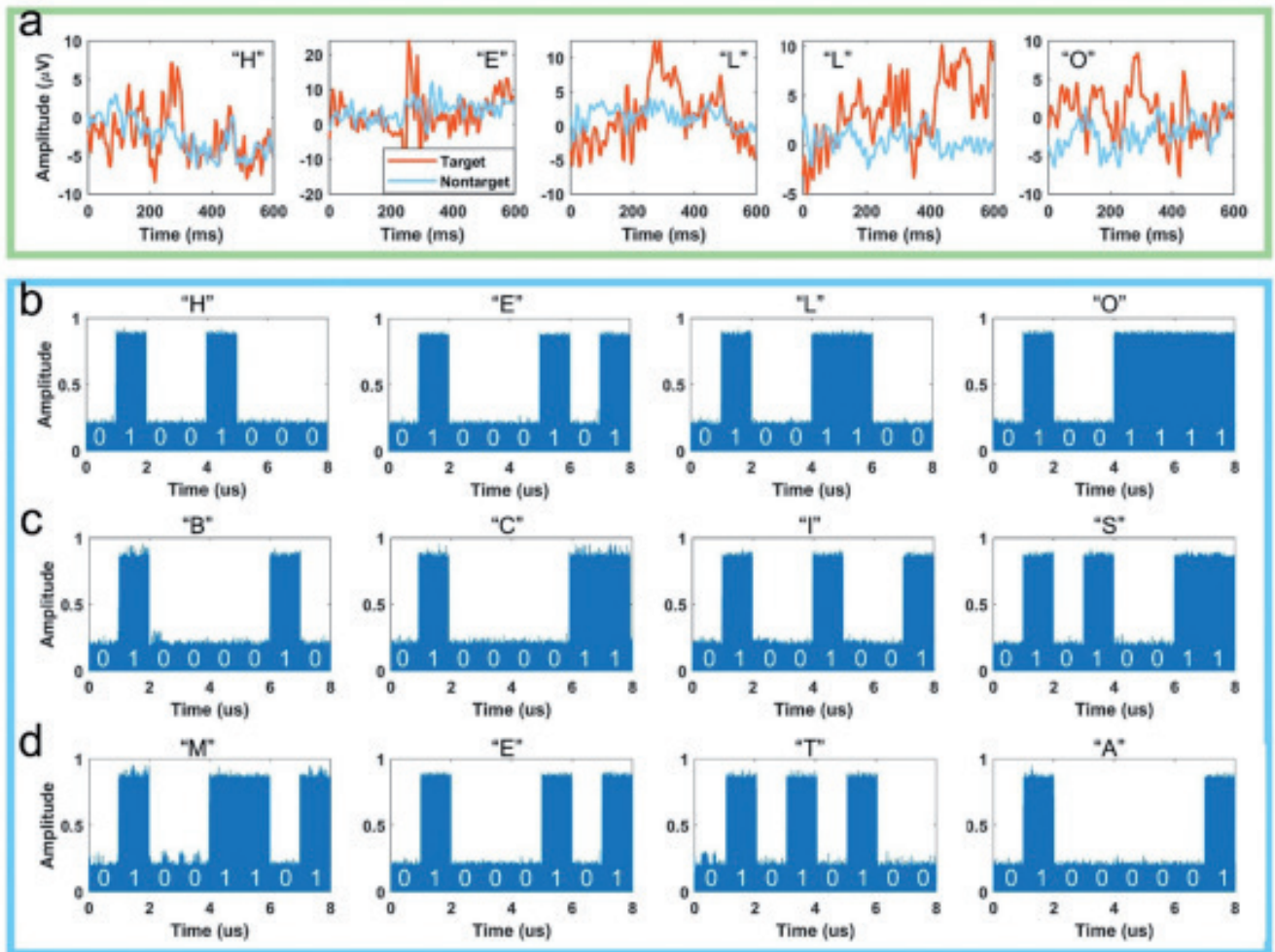


Fig. 10. Experimental results of wireless text communication using EBCM [31]: (a) Experimentally measured EEG signals in a text communication scheme. For demonstration, EEG segments corresponding to the five letters "HELLO" are presented. (b)-(d) Measured electromagnetic signals of the letters "HELO", "BCIS" and "META".

distance of 0.3 m, and the receiver is an antenna integrated near the receiving MF, which is connected to an LNA and a detector, as well as an ADC controlled by another FPGA. The received and demodulated letters and text are finally displayed in the developed graphical interface. The results of all experiments are presented in the additional film to [31].

In Fig. 10a shows processed EEG responses of channel 0Z to two types of stimuli (target and non-target) when the subject pronounces the word "HELLO".

In each sub-figure corresponding to a single character spelling, for each of the two stimulus types, event-related potential (ERP) waveforms are extracted using a time-locked

average of the EEG signals across all target flashes or one of the non-target buttons in a trial. Compared to non-target data, high amplitude is clearly observed around 300 ms post-stimulus. According to the EEG signals, EBCM outputs amplitude modulated electromagnetic signals of various letters using ASCII code.

To fully demonstrate the wireless communication, additionally, [31] provides 12 segments of measured electromagnetic signals including the letters "H, E, L, O, B, C, I, S, M, E, T, A" as shown in Fig. 10b-d, where high and low amplitudes respectively represent "1" and "0" in ASCII code.

The presented data is collected by an electromagnetic detector and normalized.

Each detection generates an amplitude pulse and multiple amplitude pulses to compose the data represented, where high and low amplitudes respectively represent the codes 1 and 0. The ASCII codes of these letters are clearly visible as shown in Fig. 10b-d.

5.4. WAVEFRONT SYNTHESIS USING EBCM

Additional functions of wavefront synthesis using EBCM were also explored in [31]. For this purpose, three typical applications were developed, including visual beam scanning, multiple electromagnetic modulation and

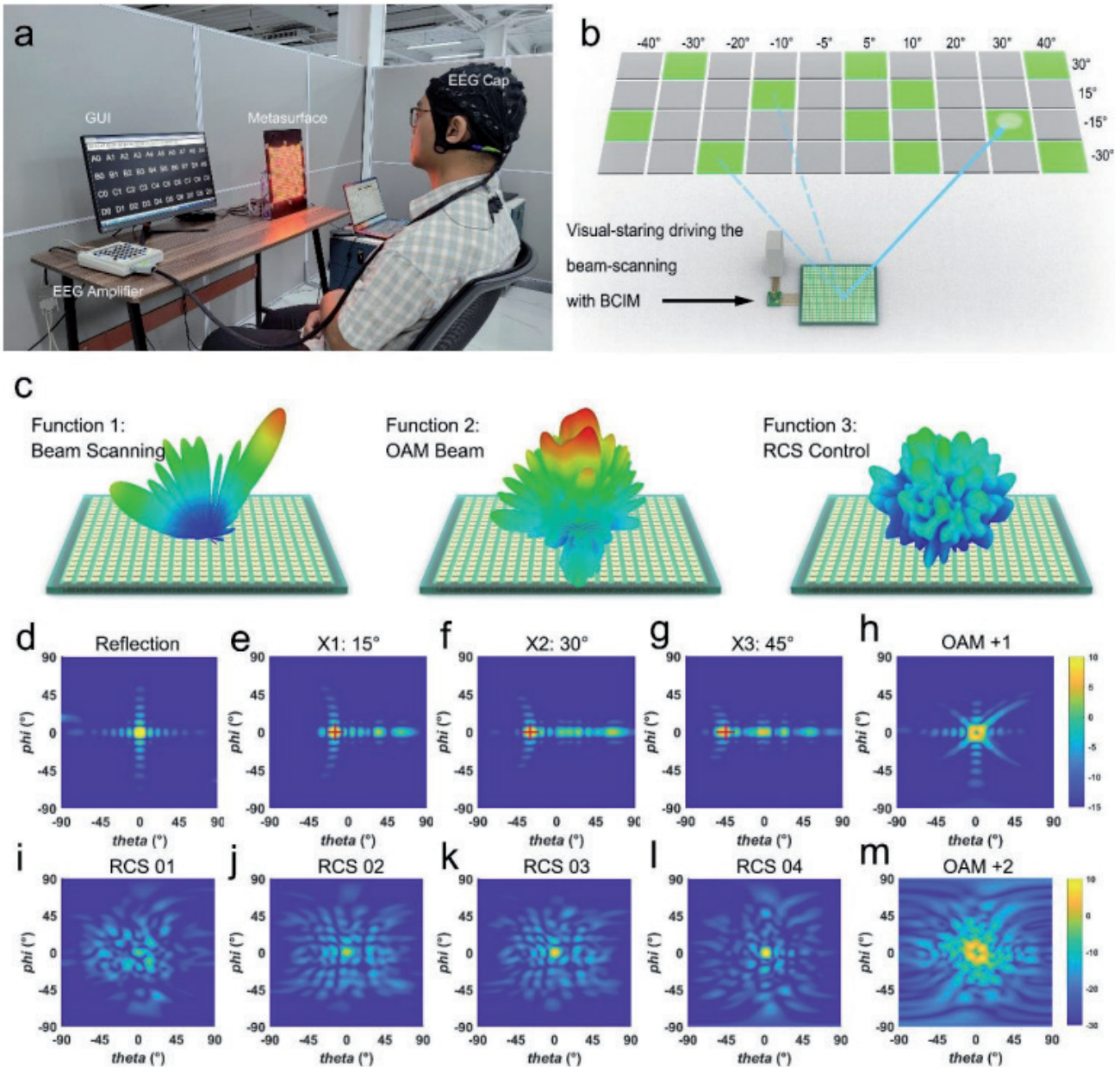


Fig. 11. Additional functions of wavefront synthesis using EBCM [31]: (a) Photo of the image encoding circuit. (b) Illustration of beam scanning using EBCM. The BCI operator's visual gaze directly controls the MP to adjust the scattering direction to the desired angle. Each button refers to a specific scattering direction. (c) Three typical electromagnetic functions including beam scanning, OAM beam generation and RCS control. (d)-(g) Simulated results of four types of beam scanning fields, where the result of the main direction measurement is marked with a red cross. The scattering beam is deflected from 0 to 450 along the x axis. (g)-(j) Results of the simulated RCS control field, where values "01" to "04" indicate four levels of reflection intensity. (k) and (l) Far-field simulation results for OAM modes +1 and +2. The central zero is clearly visible.

encoding pattern input, and an EBCM demonstration prototype was installed in which the MS was replaced by an LED version instead of a PIN diode, as shown in **Fig. 11a**.

Since the encoding patterns on the MS directly determine the electromagnetic functions, the LEDs were integrated to intuitively visualize the control of the pattern in the EBCM inspection system. In the visual beam scanning design, we want the operator to be able to appropriately control the electromagnetic beam scanning with EBCM, including beam deflections, orbital-angular momentum (OAM) beam generation, and radar cross section (RCS) control), as shown in **Fig. 11b**. A graphical interface for beam scanning was developed – **Fig. 8e**. It is expected that this scheme can be further integrated with augmented reality (AR) technology and will find more applications in adaptive mind-text wireless communication and intelligent radar detection.

The operator can now directly control the EBCM for various electromagnetic functions, including beam deflection, beam generation with OAM, and RCS control, as shown in **Fig. 11c**. The simulation results of these functions are presented in **Figs 11d-m**. For example, we illustrate the result of a vertically reflected single beam generated by a uniform phase diagram in **Fig. 11d**, and the results of three deflection angles in **Figs 11e-g**, where the simulated data clearly indicates scattering directions of 15° , 30° , and 45° , indicating great agreement with measured directions marked with a red cross. In the RCS level adjustment, the four RCS buttons "01" to "04" will generate the scatter fields shown in **Figures 11i-l**, showing scatter levels of -15 dB, -12 dB, -9 dB and -6 dB respectively. To generate the OAM beam, we observe two scattering fields of two OAM modes (+1 and +2) in **Figs 11b**

and **11m**, in which the central amplitude zero is clearly observed.

5.5. TOWARDS NEW GENERATIONS OF BIOINTELLIGENT METASURFACE SYSTEMS

Thus, based on the EBCM platform, [31] shows that the operator no longer needs any muscle action, but only looks at a specific visual button for the corresponding sequential stimulus, which can be recognized by the EBCM and converted into appropriate electromagnetic signals for communication. Three typical circuits are demonstrated with various functions, including visual beam scanning, multiple electromagnetic function switching, and MP pattern input, which contains more than 20 coding patterns for various single-beam scans, multiple beamforming, OAM beam generation, and RCS control. The presented work, combining electromagnetic wavespace and BCI, can open a new direction to explore the deep integration of metasurface, human brain intelligence and artificial intelligence to create new generations of biointelligent metasurface systems.

6. PROGRAMMABLE MS FOR WIRELESS ENCRYPTION

6.1. A SHORT INTRODUCTION

Programmable and informational MSs have demonstrated great potential in wireless communications, but there is currently little work on encrypting this communication. Although the architecture of conventional radio frequency transmitters can be significantly simplified by using the new technology presented by the author above [30,31], however, as far as we know, these studies are limited only to unprotected direct transmission of information, and research into information encryption technology based on this new type of wireless communication is still very limited. [32] proposed a programmable polarization modulated (PoM)

information MS, which can not only receive arbitrarily linearly polarized reflected waves, but also modulate their amplitudes in real time. In addition, a wireless encryption scheme is proposed by introducing a meta-key using MS programmable PoM information. The meta-key is then encoded and encrypted by hiding its codes in different polarization channels according to the encryption protocol and sent to the user using the programmable MS PoM information at the sending end. At the receiving location, a pair of polarization discriminator antennas (PDAs) are designed to receive and decode the encrypted metakey signals. Once the user obtains the metakey, the encrypted target information can be recovered. The results show that the proposed programmable PoM information MS not only can achieve good polarization modulation performance, but also shows good potentials in communication

encryption, which can greatly improve the security of wireless communication.

6.2. WIRELESS COMMUNICATION ENCRYPTION SCHEME BASED ON PROGRAMMABLE POLARIZATION-MODULATED INFORMATION MS

In **Fig. 12** shows a conceptual illustration of a wireless encryption scheme based on PoM [32]. At the transmitting end, the target image, such as the image of a lynx, is encrypted using a meta key and pre-sent by Bob – Fig. 12a. Therefore, even if the encrypted information is intercepted, it is impossible to decrypt it without the metakey. However, in order for Alice to obtain the correct information about the target, the meta key must also be sent to Alice in a secure manner, excluding the encrypted information about the target, and this operation can be implemented using PoM, as shown in Fig. 12b. The MP is loaded with PIN diodes, and its amplitude and

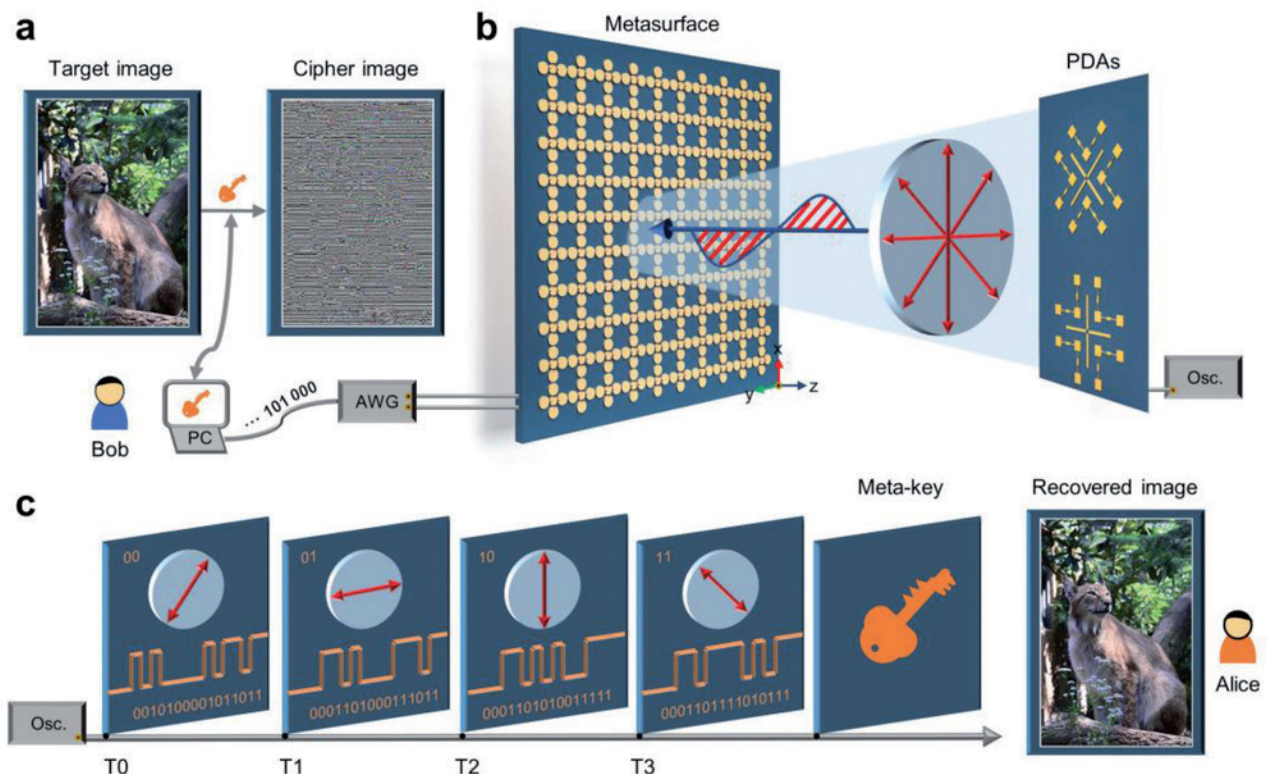


Fig. 12. Conceptual illustration of a wireless encryption scheme based on PoM [32]: a) The target image is encrypted using a meta-key to create an encrypted image. b) The voltage-controlled PoM encrypts and sends the metakey, and a pair of polarization discrimination antennas connected to the oscilloscope receives and identifies the signals. c) The meta key is decrypted by the signals received from four different polarization channels, and then the target encrypted image can be recovered using the meta key. (Photo: Hai Lin Wang, Southeast University)

reflection phase in the vertical and horizontal directions can be independently controlled in real time by adjusting the state of the PIN diodes. Therefore, when an incident wave with 45-degree polarization hits the MP, the polarization angle of the linearly polarized reflected wave can be arbitrarily edited. In addition, it is possible to further modulate

the amplitude of the reflected wave in each polarization channel. At the receiving point, two PDAs connected to the oscilloscope are used to receive signals (i.e., modulated reflected wave), which can not only identify the polarization state of the reflected wave, but also obtain a binary coding sequence based on amplitude shift keying into each polarization channel, as

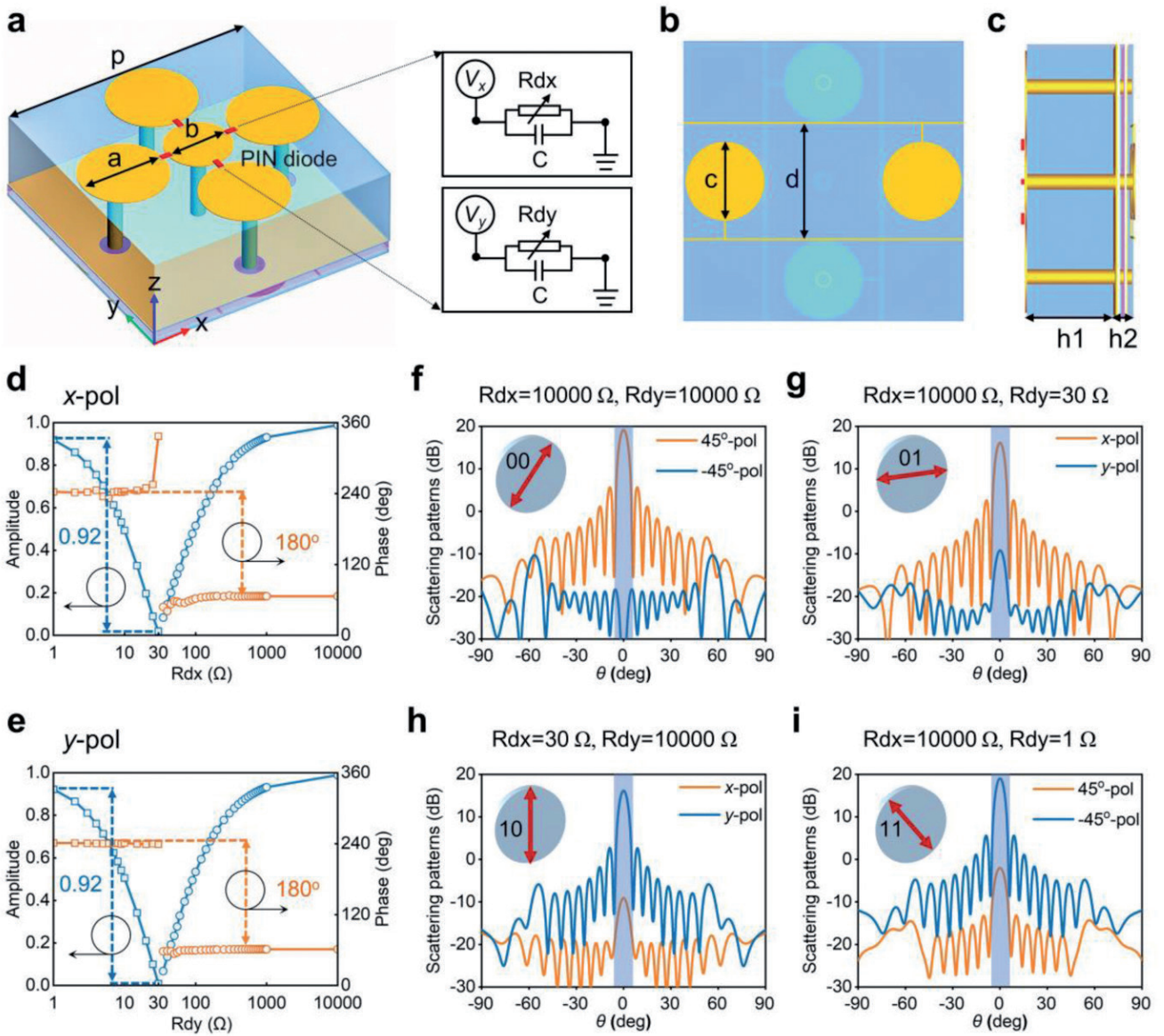


Fig. 13. Prototype design and simulation results [32]: a-c) Single PoM metasurface element loaded with four PIN diodes: a) front view, b) bottom view and c) side view. d, e) Simulated amplitudes and phases of reflection from the MF, varying with R_d at a frequency of 10 GHz: d) x-polarized wave, e) y-polarized wave. f-i) Simulated 2D far-field radiation reflection patterns for four linear polarization states: f) +45° polarization, g) x polarization, h) y polarization, i) -45° polarization. Rice. 13. Prototype design and simulation results [32]: a-c) Single PoM metasurface element loaded with four PIN diodes: a) front view, b) bottom view and c) side view. d, e) Simulated amplitudes and phases of reflection from the MF, varying with R_d at a frequency of 10 GHz: d) x-polarized wave, e) y-polarized wave. f-i) Simulated 2D far-field radiation reflection patterns for four linear polarization states: f) +45° polarization, g) x polarization, h) y polarization, i) -45° polarization.

shown in Fig. 12c. It is worth noting that these four coding sequences are transmitted using different polarization channels, and the binary metakey codes are hidden in these sequences. In this way, Alice can decode the received signal to obtain the metakey according to the agreed upon encryption protocol, and then use it to reconstruct the target image.

6.3. SIMULATION RESULTS

In Fig. 13a shows a single element of the proposed PoM [32], which consists of three metal layers separated by two dielectric substrates. Five metal round pads loaded with PIN diodes in the top layer are connected to the feed lines in the bottom layer through plated through holes so that a bias voltage can be applied to the PIN diodes. The equivalent circuit of a PIN diode (Skyworks SMP1321-040LF) is shown in the right corner of Fig. 13a. This is a parallel circuit of a constant capacitor ($C = 0.15$ pF) and a variable resistor; resistors along the x and y directions are defined as R_{dx} and R_{dy} , respectively. The values of R_{dx} and R_{dy} are controlled by the row and column bias voltages V_x and V_y , respectively, and range from 1-10,000 ohms.

Geometric parameters shown in Fig. 13a are $p = 14.2$ mm, $a = 4.4$ mm and $b = 3.6$ mm. In Fig. 13b shows the arrangement of feeder lines on the bottom layer, in which the diameter of the circular spot and the distance between two feeder lines are $c = 4$ mm and $d = 5.8$ mm, respectively. The dielectric substrates are F4B (polytetrafluoroethylene) with a relative dielectric constant of 2.2 and a loss tangent of 0.001, the thickness of which is $h_1 = 4$ mm and $h_2 = 0.254$ mm, as shown in Fig. 13c. According to [33], which proposed and experimentally demonstrated a wideband programmable MF, the amplitude and phase of the reflected electromagnetic waves can be independently controlled by adjusting the bias voltage of the meta-atom-integrated

PIN diode in real time over a wide frequency range. In Figs 13d and 13e show the simulation results of single element reflection amplitude and phase with R_{dx} and R_{dy} at 10 GHz for x - and y -polarized waveforms, respectively. The results show that the normalized amplitude of the reflected wave polarized along the x (or y) axis can be continuously controlled from 1 to 0 when R_{dx} (or R_{dy}) increases from 1 to 30 ohms or decreases from 10,000 to 30 ohms, the phase difference of the reflected waves in these two areas is around 180° . In addition, the proposed modular element also has broadband characteristics and can operate in the frequency range of 9-11 GHz.

When a 45-degree polarized wave illuminates the MS, the polarization angle of the reflected wave can be arbitrarily adjusted by controlling the amplitude and phase of the x - and y -polarization components. In Fig. 13f-i shows the simulation results of reflection waves with polarizations of 45° , x , y and -45° , where the MP consists of 20×20 elements with a total size of 284×284 mm². When the resistances of the PIN diodes in the x and y directions are set to $R_{dx} = R_{dy} = 10000$ ohms, both the x and y polarization components are effectively reflected and have the same amplitude and phase, so the reflected wave has the same polarization as the incident wave, that is, a polarization of 45° , as shown in Fig. 2f. When the resistances of the PIN diodes in the x and y directions are set to $R_{dx} = 10000$ ohms and $R_{dy} = 30$ ohms respectively, only the x polarization component is effectively reflected, while the y polarization component is completely absorbed, so the reflected wave will be of x polarization, as shown in Fig. 2g. Similarly, when the resistances of the PIN diodes in the x and y directions are set to $R_{dx} = 30$ ohms and $R_{dy} = 10000$ ohms respectively, only the y polarization component is

effectively reflected, while the x polarization component is completely absorbed, the reflected waves will be y -polarized, as shown in Fig. 2*b*. However, when the resistances of the PIN diodes in the x and y directions are set to $R_{dx} = 10000$ ohms and $R_{dy} = 1$ ohms respectively, the x and y polarization components are effectively reflected with the same amplitude but have a phase difference of 180° , so the reflected wave will be cross-polarized incident wave, that is, polarization -45° , as shown in Fig. 2*i*. It is worth noting that although only four special cases are

demonstrated, a reflected wave with an arbitrary polarization angle can be obtained by precisely controlling the amplitude and phase of the x - and y -components of the reflection. In [32], the encryption scheme uses polarization channels of 45° , x , y and -45° , which are encoded as polarization codes "00", "01", "10" and "11", respectively. In addition, when a left-handed circularly polarized wave illuminates the MS, the polarization ellipticity of its reflected wave can also be arbitrarily tuned by controlling the amplitude and phase of the x - and y -polarization components.

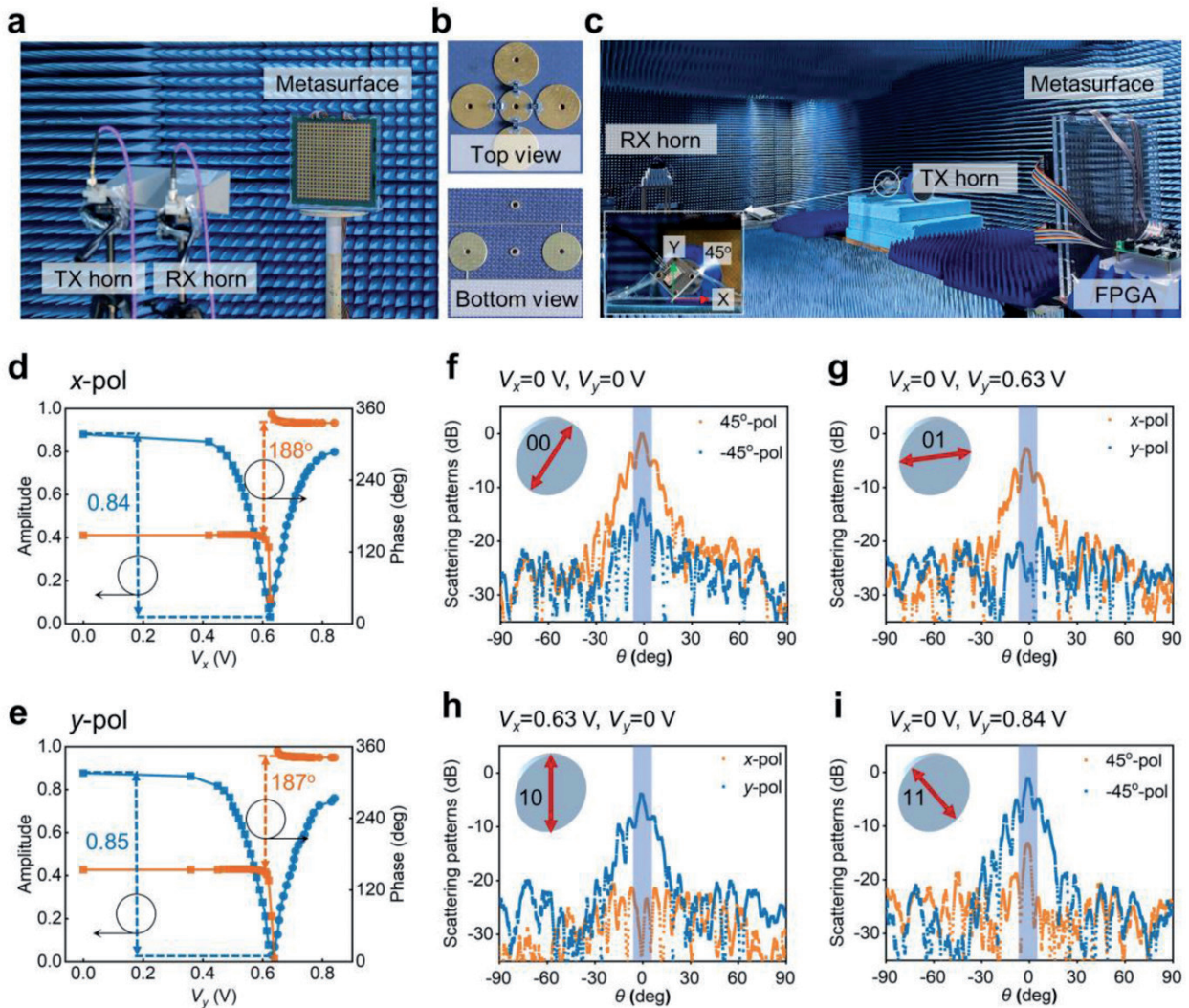


Fig. 14. Experimental results of MP PoM [32]: a) Experimental setup for measuring reflection coefficients in an anechoic chamber. b) Top and bottom views of one block element. c) Measurement of MP characteristics. d, e) Measured amplitudes and phases of reflection from the MF at various bias voltages when probing with d) x -polarized and e) y -polarized waves at a frequency of 10 GHz. f-i) Measured 2D radiation patterns for four linear polarization states: f) 45° polarization, g) x polarization, h) y polarization and i) -45° polarization.

6.4. MEASUREMENT RESULTS

The programmable information MP PoM is fabricated and measured in an anechoic chamber [32], as shown in Fig. 14, where the metasurface consists of 20×20 elements with a total size of 284×284 mm², and the PIN diodes along the horizontal and vertical directions are independently driven by two bias voltages. In Fig. 14a shows an experimental setup for measuring the amplitude and phase of reflection, in which two rectangular horn antennas are placed at a distance of 1.5 m from the MP to emit and receive signals, respectively. A photograph of one of the blocks is shown in Fig. 14b, which shows the block element loaded with PIN diodes at the top, and the structure of the feed lines at the bottom. In Fig. 14d shows the amplitude and phase measurements of the x -polarized reflection wave at 10 GHz. When the bias

voltage V_x continuously changes from 0 to 0.84 V, the amplitude of the reflected wave can be continuously adjusted from 0.02 to 0.87, and the phase can be independently switched between the two phases with a difference of about 188° . A similar result can be obtained for a y -polarized wave, as shown in Fig. 14e. The measurement results are in good agreement with the simulation results shown in Fig. 13c,d. In addition, the broadband characteristics of the MP were also confirmed by measurements. The far-field radiation patterns of the PoM are measured in a standard microwave anechoic chamber to test the effectiveness of polarization modulation, as shown in Fig. 14c. The MP is placed on a rotating platform, and an x -band metamaterial lens antenna is placed at a distance of 80 cm from the MP to generate an incident plane wave with 45° polarization. A standard x -band rectangular

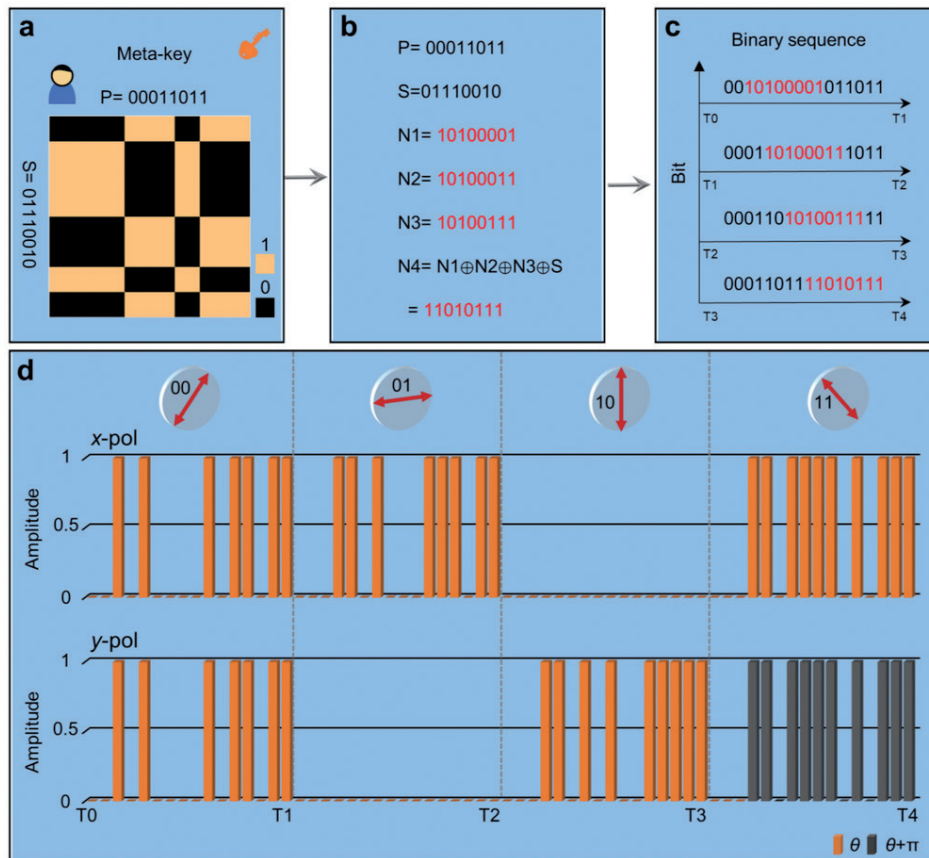


Fig. 15. Encryption process of wireless communication scheme with PoM encryption [32]: a-c) Encryption process with four binary sequences as meta-key. d) Two orthogonal input voltage signals of x - and y -polarized waves at different linear polarization channels, respectively.

horn antenna is mounted on the other side of the anechoic chamber as a receiver, where the distance between the receiving horn antenna and the rotating platform is about 10 m. The measured far-field radiation patterns of various linearly polarized reflected waves at different bias voltages are shown in Fig. 14*f-i*. When the PIN diode bias voltages in the x and y directions are set to $V_x/V_y = 0/0$, $0/0.63$ V, 0.63 V/ 0 and $0/0.84$ V, the reflected wave will have a polarization of 45° , x , y and -45° respectively.

6.5. METAKEY BASED ON MS PoM

The block diagram of metakey encryption based on MS PoM is shown in Fig. 15 [32]. A metakey consists of two 8-bit binary numbers P and S (Fig. 15*a*), in which the Mth row and Nth column element of the metakey matrix are achieved by XORing the Mth element of S and the Nth element P.

In Fig. 15*b* shows the encoding rule of P and S. In this encryption scheme, P is encoded as 00011011, representing information about the polarization channels, in which the codes "00", "01", "10" and "11" correspond to the polarization channels 45° , x , y and -45° respectively. S can be any binary sequence, which in this case is encoded as the 8-bit binary number 01110010. To avoid the information of S being easily intercepted, [32] introduces four other 8-bit binary numbers N1, N2, N3 and N4, in which N1, N2 and N3 can be random 8-bit binary numbers, and $N4 = S \oplus N1 \oplus N2 \oplus N3$ (" \oplus " is an exclusive OR symbol). To further enhance the security of the metakey, we insert N1, N2, N3 and N4 into the P sequence respectively to generate four 16-bit binary sequences in which N1, N2, N3 and N4 are inserted after the polarization channel codes "00", "01", "10" and "11" respectively, and then these four 16-bit binary numbers are sent cyclically in turn using the appropriate polarization channel through the PoM MS,

as shown in Fig. 15*c*. Taking the polarization channel x as an example, $N2 = 10100011$ is inserted after the "01" P code to generate a new 16-bit binary number 0001101000111011, which is sent using the polarization channel x during the time period T1–T2. For this 16-bit binary number, we redefine the values of the codes "0" and "1", which represent the low and high level signals corresponding to the amplitude of the electromagnetic wave in each polarization channel, that is, low reflection represents code "0" and high reflection – code "1".

In Fig. 15*d* shows the desired amplitude and phase distributions of the x - and y -polarized waves relative to the corresponding coding sequence in each polarization channel during the time interval T0–T4. It is worth noting that the height of the cuboid represents the amplitude of the electromagnetic waves, and the orange and black colors indicate that their phases are θ and $\theta + \pi$, respectively. Taking a 45° polarized channel as an example, the amplitude and phase of the x - and y -polarized waves must be the same to provide a 45° polarized electromagnetic wave, and then the amplitude of the 45° polarized electromagnetic wave is further modulated to change with time, generating the required coding sequence 0010100001011011, as shown in the time period T0–T1 in Fig. 15*d*. Coding sequences in other polarization channels are implemented using a similar method, which is also shown in Fig. 15*d*.

6.6. IMPLEMENTATION OF A WIRELESS COMMUNICATION SYSTEM WITH PoM ENCRYPTION

A wireless communication system was built based on the proposed PoM to implement the above-mentioned encryption scheme in an indoor scenario, as shown in Fig. 16*a* [32]. It consists of a transmitting module and a receiving module, in which the transmitting

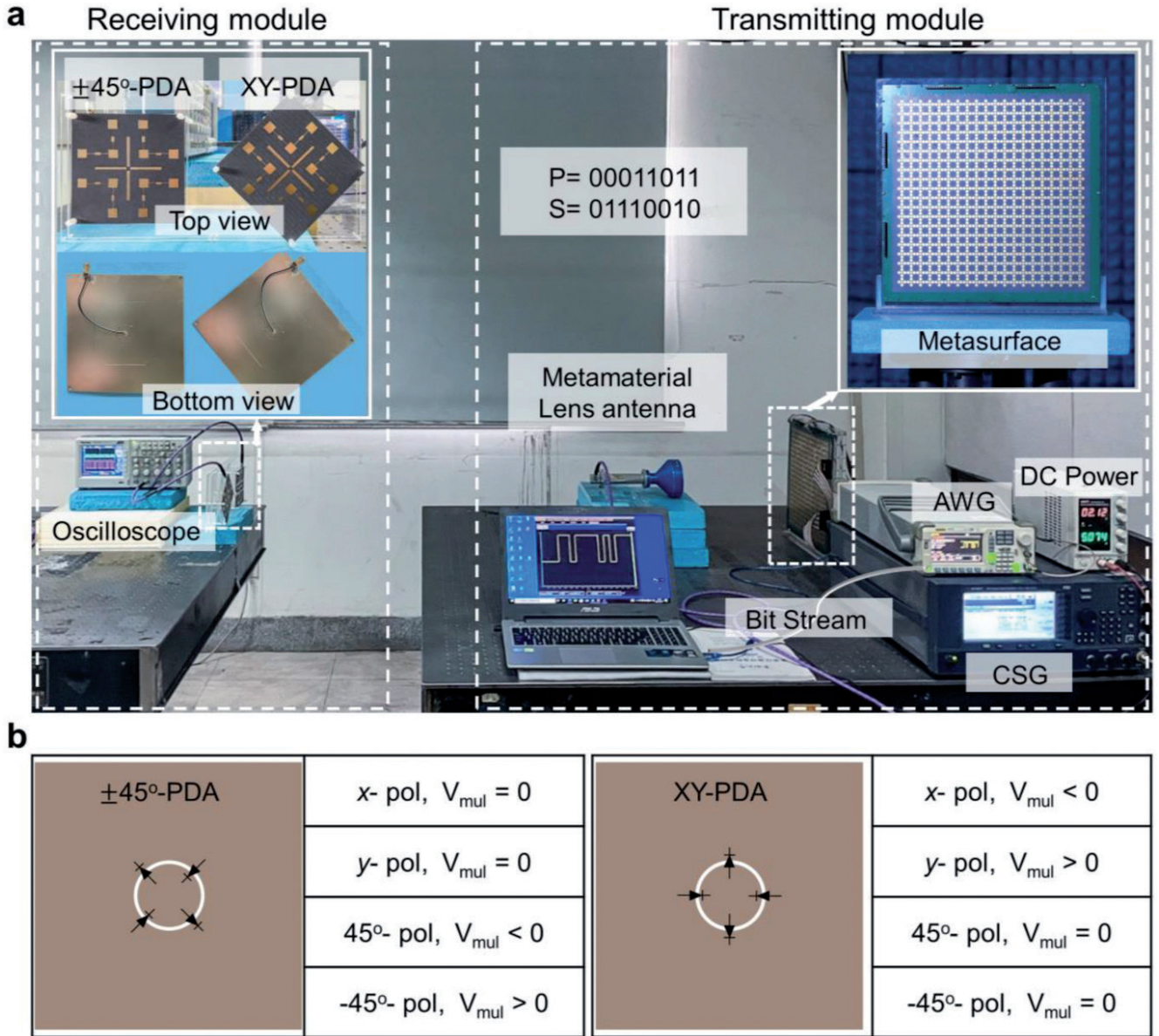


Fig. 16. Experimental setup of PoM wireless communication system [32]: a) System testbed, MP photos and top and bottom view photos $\pm 45^\circ$ -PDA and XY-PDA, respectively. b) Output voltages of two PDAs in different states of linear polarization.

module consists of a metamaterial lens antenna, a PoM MP, a carrier signal generator (Keysight E8267D), a spectrum analyzer (Keysight N9040B), an arbitrary waveform generator (AWG) (Rigol DG5101), and a stabilized DC power supply, and the receiving module consists of an oscilloscope and a pair of polarization discriminator antennas (PDAs). In the transmitting module, a metamaterial lens antenna is placed at a distance of 35 cm from the MP to generate an incident plane wave with 45 degree polarization, which can

be considered as a carrier with an operating frequency f ; A stabilized AWG DC power supply is connected to the MP to supply bias voltage to the PIN diodes. It is worth noting that two AWGs were required to provide row- and column-adjustable offset voltages for the real-time MP, respectively, but since there was only one AWG, the experiment uses a stabilized source instead of another AWG DC power supply. A time-varying bias voltage is applied to the MP through the AWG to realize real-time modulation of the polarization and amplitude

of the reflected wave to obtain the desired polarization channel and its corresponding coding sequence.

In the receiving module, at a distance of 160 cm from the PoM MP, a pair of PDAs are placed to receive the signal, which are connected to a two-channel oscilloscope. PDA photos are displayed in the upper left corner of Fig. 16a, on which two PDAs are placed with a relative rotation angle of 45°, named ±45°-PDA and XY-PDA, respectively. On the rear panel of the PDA, four zero-bias Schottky diodes (SMS7621-040LF) are loaded onto a slot ring to implement a dual balanced RF multiplier. When PDAs receive signals, the polarization

state of the signal can be first determined by the output voltage of the two PDAs, as shown in Fig. 16b. Specifically, if the output voltages ±45°-PDA and XY-PDA are large negative (or positive) and zero, respectively, the signal will have a polarization of 45° (or -45°), and if the output voltages ±45°-PDA and XY-PDA are equal to zero and a large negative (or positive) value, respectively, the signal will be *x*- or *y*-polarized. Once the polarization state of the signal is determined, the corresponding coding sequence of "0" and "1" in each polarization channel can be further obtained using the low and high level output voltages detected by the oscilloscope.

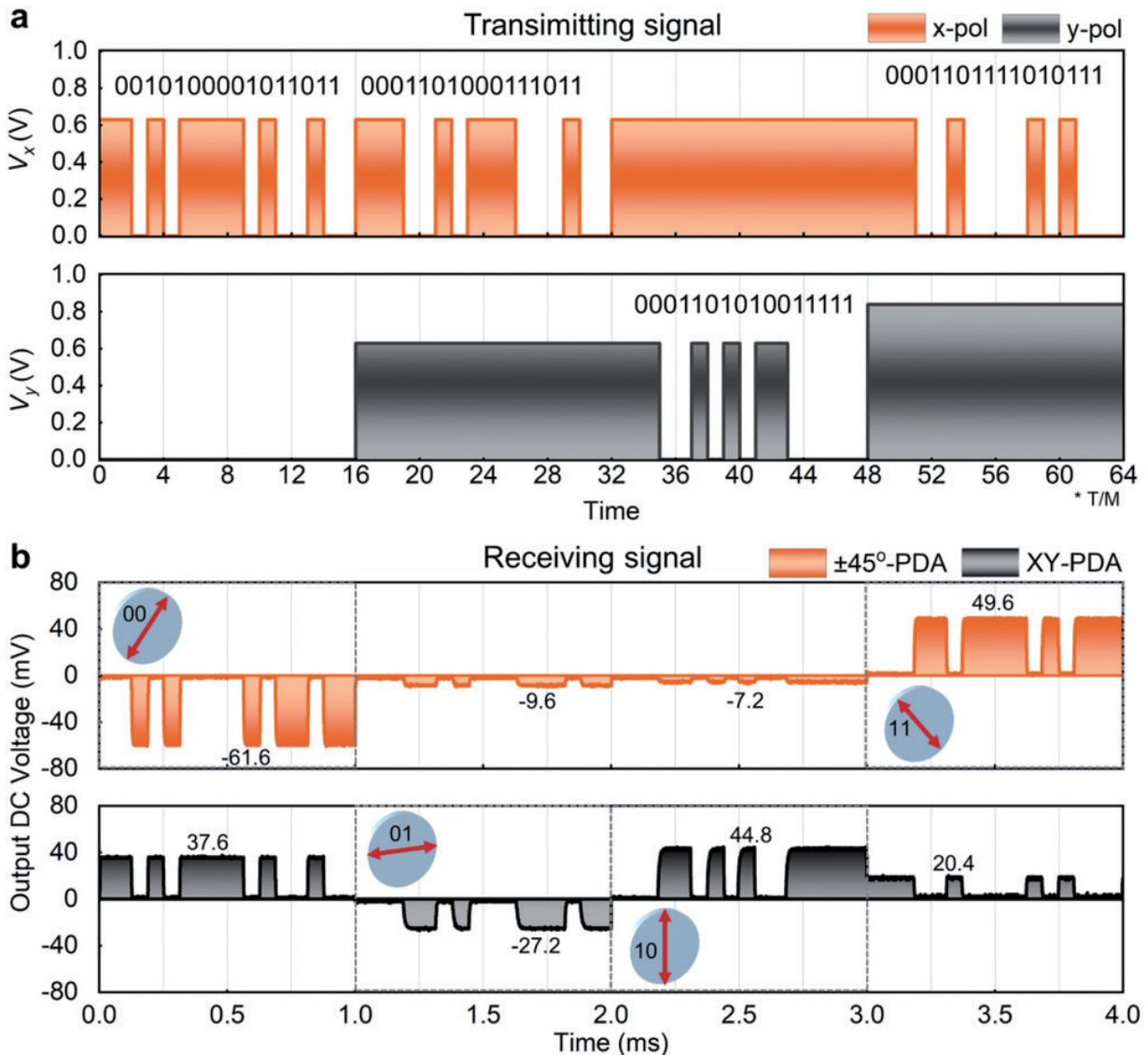


Fig. 17. Shapes of transmitting and receiving signals [32]: a) Time-varying bias voltages of the AWG module for controlling the PoM MP. b) Measured DC output voltages of two PDAs under AWG control.

6.7. DECODING FEATURES

In Fig. 17a shows the time-varying sequences of the AWG bias voltage and the regulated DC power supply in the MP PoM control experiment, in which 0.63 V corresponds to low reflection, and 0 and 0.84 V correspond to high reflection, but their phase difference is 180°.

The time interval for each code is $T/M = 0.0625$ ms ($T = 4$ ms, $M = 64$), so the transmission data rate is 16 kHz, and the maximum data rate mainly depends on the AWG modulation speed and PIN diode switching speed. It should be noted that one of the bias voltages (V_x or V_y) remains unchanged in each polarization channel, since in the experiment it is provided by a stabilized constant current source. In Fig. 17b shows the $\pm 45^\circ$ -PDA and XY-PDA output voltages measured by the oscilloscope at four different time periods. The polarization of the signal can first be identified by the relationship between the $\pm 45^\circ$ -PDA and XY-PDA output voltages according to the rule shown in Fig. 16b. So we can know that the signals shown in Fig. 17b, have a polarization of 45° , x -, y - and -45° from left to right. It is worth noting that the signal received by the XY-PDA is much greater than zero in the 45° ("00") and -45° ("11") polarization channels, which should be close to zero, as shown in Fig. 16b. The reason for this result is that the bias voltage for driving the y -polarized wave in these two cases is provided by a regulated DC power supply, which is set to a fixed voltage of 0 and 0.84 V, respectively, so the y -polarization component cannot be eliminated. This problem can be solved by using a different arbitrary waveform generator instead of a regulated DC power supply. Knowing the polarization channels, in accordance with the encryption protocol shown in Fig. 15, we can extract N1, N2, N3 and N4 after the codes "00" in the 45° polarization channel, "01" in the x -polarization channel, "10" in the y -polarization channel, and "11" in the -45° polarization channel, respectively. Additionally, we can determine whether the extraction results are correct by checking whether the remaining 8-bit binary numbers in all channels are equal

to $P = 00011011$. S can then be obtained using a bitwise exclusive OR operation on N1, N2, N3 and N4. Therefore, according to the above rules, the binary encoding streams 0010100001011011, 0001101000111011, 0001101010011111 and 0001101111010111 in four different polarization channels can be first read out from the measurement results shown in Fig. 17b, respectively, and then N1 = 10100001, N2 = 10100011, N3 = 10100111 and N4 = 11010111 can be further extracted to obtain the final $P = 00011011$ and $S = N1 \oplus N2 \oplus N3 \oplus N4 = 01110010$. The metakey matrix can then be obtained by performing the operation exclusive OR for P and S, as shown in Fig. 15a. Finally, the encrypted lynx image can be recovered using the meta key.

In addition, the fault-tolerant performance of the metakey was further investigated in [32]. The results show that the target image can also be approximately observed if there is only one or two bit error in the receiving process N1 – N4, but the image resolution will become lower and lower as the bit error rate increases, and the image becomes completely unrecognizable when the number error codes reach four – Fig. 18, where *incorrect characters are highlighted by hand* [32].

Thus, in [32], a programmable information MP PoM is proposed and its application for encrypting wireless communications using

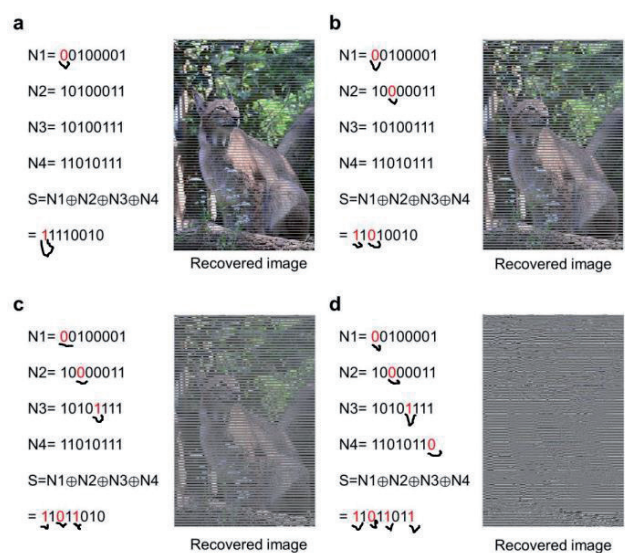


Fig. 18. Recovered image with an incorrect metakey [32]: a) Single-bit error. b) Two-bit error. c) Three-bit error. d) Four-bit error.

a metakey is shown. In this scheme, the metakey is sent to the user independently in real time and can be dynamically configured for different messages to improve security. A wireless communication system including transmitting and receiving modules was also built to demonstrate the feasibility of the encryption scheme. This approach offers a low-cost solution for implementing a PoM encrypted wireless communication network that does not require antenna arrays, filters, or mixers. The work [32] presents a new concept of information transmission based on programmable MS, which can find great potential in the next generation of information encryption.

7. OPTICAL ENCRYPTION AT SPATIAL FREQUENCIES USING MS

7.1. INTRODUCTORY PART

In Section 4 of this work, there was already a discussion about optical encryption of information using MS. Here we can only notice that for most MS-based encryption methods, information is encrypted in the MS of physical forms, which limits information exchange and compatibility with digital information processing technology. However, both Fourier space and real space can be simultaneously used as encryption channels.

An alternative optical encryption scheme with MPs operating as analog optical information processors for optical images was proposed and experimentally demonstrated in [34]. Thus, information can be conveniently transmitted, decrypted and processed using images in software, as opposed to hardware MSs. This is achieved by modulating the spatial frequencies of MP optical images. It was confirmed in [34] that both the intensity and the spatial frequency phase of the light field can be modulated by MS to encode information. The information can then be obtained by performing a Fourier transform

on the encrypted images. In addition, it has been shown that spatial frequencies of optical images can provide sufficient channels to increase information capacity. Since the information can be simply and directly linked to the MS, the proposed scheme can also avoid the careful design of the MS using a complex algorithm in the traditional metasurface hologram. Most importantly, since information is encrypted in non-MS images, information exchange is more flexible, even compatible with modern information processing technologies. Therefore, the proposed method may offer another promising platform for MS optical encryption.

7.2. WORKING PRINCIPLES

As shown in **Fig. 19a** [34], considering the case where an object is illuminated by a coherent laser beam, the resulting two-dimensional light field pattern as an optical image can be expressed in terms of its field.

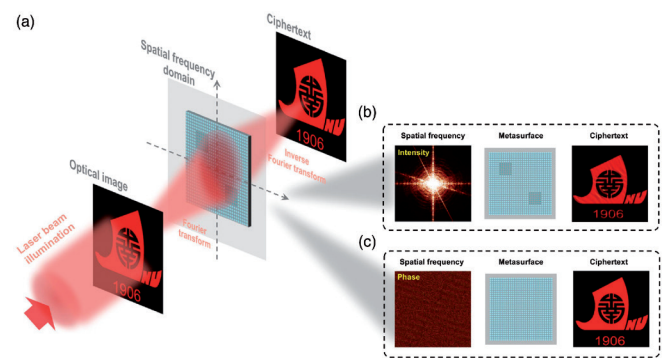


Fig. 19. Concept of spatial frequency encryption [34]: (a) Diagram of the optical encryption process. An optical image as an information carrier is obtained under laser illumination, and access to its spatial frequency region can be obtained after the Fourier transform. The information to be encrypted is loaded into the spatial frequency domain using MS, and the image of the ciphertext is obtained using the inverse Fourier transform. (b) Intensity encryption for spatial frequency. Different spatial frequency components can be changed by adjusting the transmission of different subdomains (light and dark colors) of the MS. The output ciphertext is similar to the input optical image with a slight difference. (c) Phase encryption for spatial frequency. The information is encrypted by introducing phase differences into the spatial frequency using MS.

Intuitively, information may be encrypted directly in the image, but it can be easily decrypted. To increase security, we will encrypt information in the spatial frequency domain of images, which is different from the domain of the real image. This can be achieved by applying a Fourier transform operation to the input optical image, then encrypting the information using MS, and finally obtaining an encrypted optical image by inverse Fourier transform. This process can be briefly expressed as:

$$\tilde{E}_{out}(x, y) = F^{-1}\{\tilde{h}(u, v) \cdot F[\tilde{E}_{in}(x, y)]\}, \quad (1)$$

where \tilde{E}_{out} is the electric field of the encrypted optical image, F and F^{-1} are the forward and inverse Fourier transform operators, $\tilde{h}(u, v)$ is the optical transfer function (OTF) constructed by the MS in the spatial frequency domain.

The information to be encrypted can be directly represented by the MS in the form of OTF, and then transmitted by modulating the spatial frequencies of the optical image. Thus, it is almost impossible to obtain information by observing only the image of the ciphertext. On the contrary, only through proper analysis of the changed spatial frequency of the image can information be obtained. It should be noted that the light nature of the spatial frequencies of optical images provides different encryption channels that can be conveniently adapted by MSs supporting different OTFs $\tilde{h}(u, v)$. For example, the complex function constructed by MS $\tilde{h}(u, v)$ provides two modulating degrees of freedom, namely, intensity and phase for encryption, as schematically shown in Fig. 19b and 19c. Intensity modulation $\tilde{h}(u, v)$ is simple and convenient, phase modulation $\tilde{h}(u, v)$ can improve safety. It should also be noted that $\tilde{h}(u, v)$ this is a function of spatial frequency and therefore provides another encryption channel in which different spatial

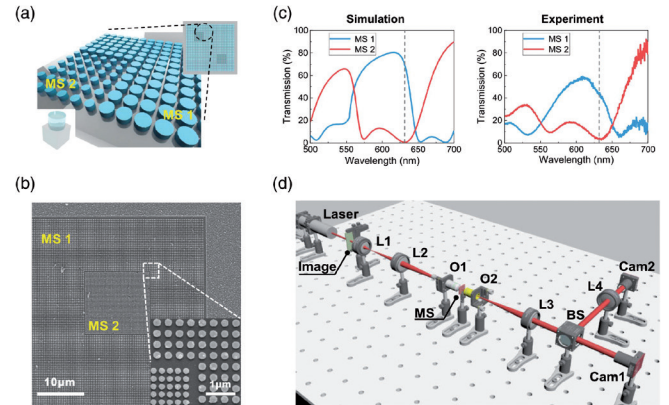


Fig. 20. MS for intensity encryption and experimental setup for encryption [34]: (a) Schematic of MS with different transmission in different regions for MS 1 and MS 2. (b) SEM image showing part of the fabricated MT. (c) Simulated and experimental transmission spectra of different MS regions. The gray dotted line indicates the target wavelength of 633 nm. (d) Experimental setup for implementing the proposed optical encryption. Here L1 – L4 are lenses; O1 and O2 – lenses; MS – MS metasurface; BS – beam splitter; Cam1 and Cam2 are cameras.

frequencies can be tuned separately using the MS, increasing information capacity.

7.3. SIGNAL INTENSITY ENCRYPTION IN THE SPATIAL FREQUENCY DOMAIN

In practice, the intensity of the spatial frequency signal can be modulated by controlling the MS transmission. For this purpose, [34] designed and fabricated a silicon MS with different transmittances in different regions, which are designated as MS 1 and MS 2 in Fig. 20a. The transmittance can be adjusted simply by changing the periods and radii of the silicon nanopillars on the silica substrate.

Images of the fabricated MS obtained using scanning electron microscopy (SEM) are presented in Fig. 20b. Region MS 1 contains 200×200 units measuring about $75 \times 75 \mu\text{m}$, and region MS 2 includes 50×50 units measuring about $15 \times 15 \mu\text{m}$. In Fig. 20c shows that at a given wavelength of 633 nm, large transmittance contrast between different regions can be obtained. This means that the MS can appropriately modulate the intensities of spatial frequencies in

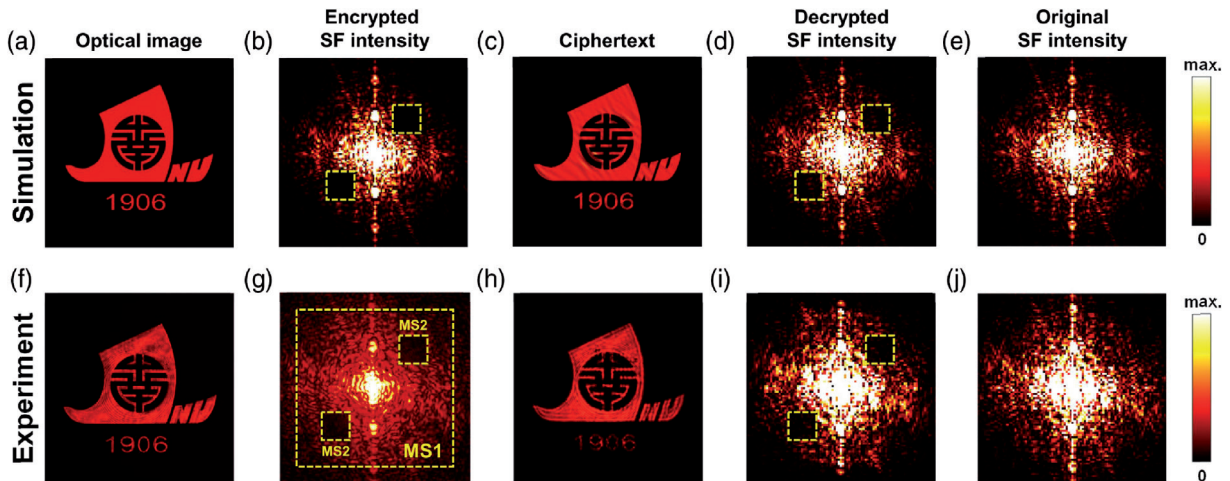


Fig. 21. Results of modeling and experiment on encryption and decryption of the spatial frequency intensity of an optical image [34]: (a) Optical image as an information carrier. (b) Spatial frequency intensity distribution after encryption. The two yellow dotted rectangles indicate encrypted areas. (c) Output image of the ciphertext after encryption. (d) Spatial frequency intensity distribution after decoding. The yellow dotted lines serve as a guide to indicate encrypted areas. (e) Spatial frequency intensity distribution before decoding. (f)-(j) Corresponding experimental results..

individual regions when it is placed in the spatial frequency region of an optical image. Therefore, information can be encrypted into an optical image using MS. For example, information about the null state or square pattern can be represented by erasing the spatial frequency in the lower transmission region. To encrypt information, we have developed a microscopic experimental setup of Fourier optics, as shown in Fig. 20d. With this setup, we can project the spatial frequency spectrum of the optical image onto the MS and capture both the modulated spatial frequency intensity and the output encrypted image, validating the proposed encryption method.

The results of encryption by intensity are presented in Fig. 21 [34]. As the media image, we select the Jinan University logo, which is shown in Fig. 21a [10,34]. Numerically, we can obtain a picture of the intensity of its spatial frequency using the Fourier transform. Information can be encrypted by spatial frequency by deliberately setting the value to zero in some spatial regions, as shown by the two yellow dashed lines in Fig. 21b. After

this, we can get the ciphertext image shown in Fig. 21 with inverse Fourier transform.

Although we artificially changed the spatial frequency, the encrypted image is still similar to the original one, except that some ripples have appeared. Finding encrypted information directly from an image is difficult, unless you apply a Fourier transform to it, as in the decryption process, the result of which is shown in Fig. 21d. For ease of comparison, we present the spatial frequency intensity picture before encryption in Fig. 21e. The two encrypted regions can be easily identified by comparing the patterns before and after encryption, indicating the feasibility of the method.

To demonstrate the proposed optical encryption method, corresponding experiments were carried out. The input optical image shown in Fig. 21f, obtained by illuminating an etched pattern on a gold film with a laser beam. The spatial frequency of the image can be generated using a lens performing a Fourier transform and then projected onto the MS. Since the transmittances are different in different areas of the MS, the spatial frequency is modulated

accordingly, as shown in Fig. 21g. Most of the light can pass through the high transmittance region of MS 1, while the low transmittance regions of MS 2 will be blocked. Therefore, information can be successfully encrypted in spatial frequency. Using another lens for the inverse Fourier transform, we can obtain the encrypted image shown in Fig. 21b. Encrypted information is difficult to find directly from the encrypted image. It is important to note that the encrypted image and encrypted information can be flexibly delivered without a hardware metasurface carrier. Once the encrypted image is received, the information can be decrypted using a numerical Fourier transform on a computer – Fig. 21i. Also shown is the experimental result of the intensity pattern before encryption in Fig. 21j for comparison. It should be noted that the location and area of MS 2 areas are not strictly limited and can be changed according to practical needs.

7.4. PHASE ENCRYPTION AT SPATIAL FREQUENCY

In practice, the security of intensity encryption is not high enough because the information can be directly decrypted by applying a Fourier transform, and then the intensity pattern can be easily identified. In contrast, the spatial frequency phase pattern usually has a random distribution, and the original phase pattern before encryption is needed as a decryption key, which is a promising degree of freedom for encryption with higher security compared to intensity encryption. It was shown in [34] that the encryption method discussed above for intensity can also be applied to spatial frequency phase, except that phase MS is used as an alternative. The designed phase MS is shown schematically in Fig. 22a, which consists of identical silicon nanopillars on a silica substrate. The periods and radii of nanopillars differ from those in MS used in intensity encryption. The phase MS is

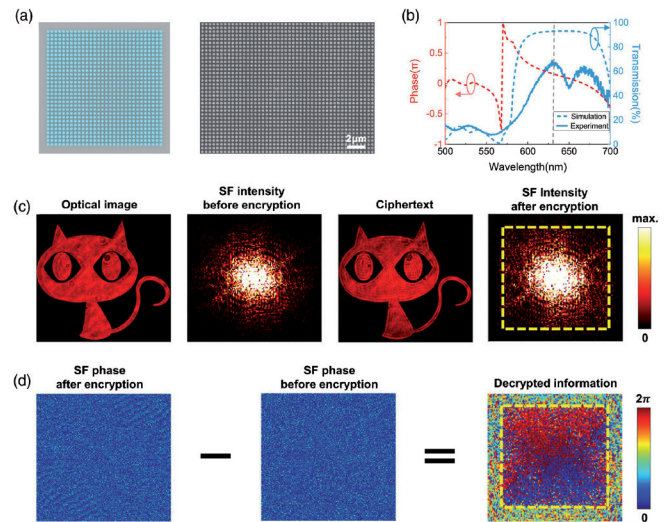


Fig. 22. Phase MS and experimental results of phase encryption and decryption [34]: (a) Schematic and SEM image of the phase MS. (b) Model (dashed blue line) and experimental (solid blue line) transmission spectra, as well as model phase spectrum (dashed red line) of the phase MS. (c) Optical images and corresponding spatial frequency intensity distributions before and after encryption. The yellow dotted frame indicates the encrypted area. (d) Phase distribution of spatial frequency before and after encryption. Decoding consists of extracting the phase difference between them.

also coated with a thick layer of polymethyl methacrylate (PMMA). The entire MS contains 200×200 units with a size of about $75 \times 75 \mu\text{m}$. In Fig. 22b shows both simulated and experimental MF transmission spectra. The transmittance at 633 nm is relatively high, resulting in the smallest possible intensity variation. It is important to note that the phase difference is introduced by the MS relative to the environment. To conduct phase encryption experiments, the same experimental setup was used as for intensity encryption, except for the substitution of MS. After encrypting the input phase-MS optical image, we captured the encrypted optical image and then numerically applied the Fourier transform operation to it. In this way, we can obtain both the intensity and the phase distribution of the spatial frequency for decoding.

The subsequent encryption results are shown in Fig. 22c and 22d. The output encrypted image and its spatial frequency intensity distribution after encryption are similar to the input optical image and intensity distribution before encryption. This means that encrypted information is difficult to identify directly or by applying a Fourier transform and then observing the intensity pattern, unlike in the case of intensity encryption. In addition, it is also difficult to find the encrypted information by examining the phase distribution of the spatial frequency due to its randomness, as shown in Fig. 22d. To decrypt the hidden information, it is necessary to extract the phase difference between the spatial frequencies before and after encryption, since the MS contributes mainly to the phase difference. Therefore, without the key of the original image, decryption is a huge

problem, which improves security compared to the case of intensity encryption.

7.5. SPATIAL FREQUENCY MULTIPLEXING TO INCREASE ENCRYPTION CAPACITY

Increasing the number of information channels is an important topic in the study of optical encryption. In the proposed method, even a single image can provide multiple channels due to the abundance of spatial frequencies. In principle, each spatial frequency can act as one channel, but this is usually limited by the received spatial frequency range and other practical conditions. However, in [34] it was proven that a certain range of spatial frequencies can be used as one information channel. In Fig. 23 shows one of the encryption rules and corresponding experimental results based on the phase encryption demonstrated

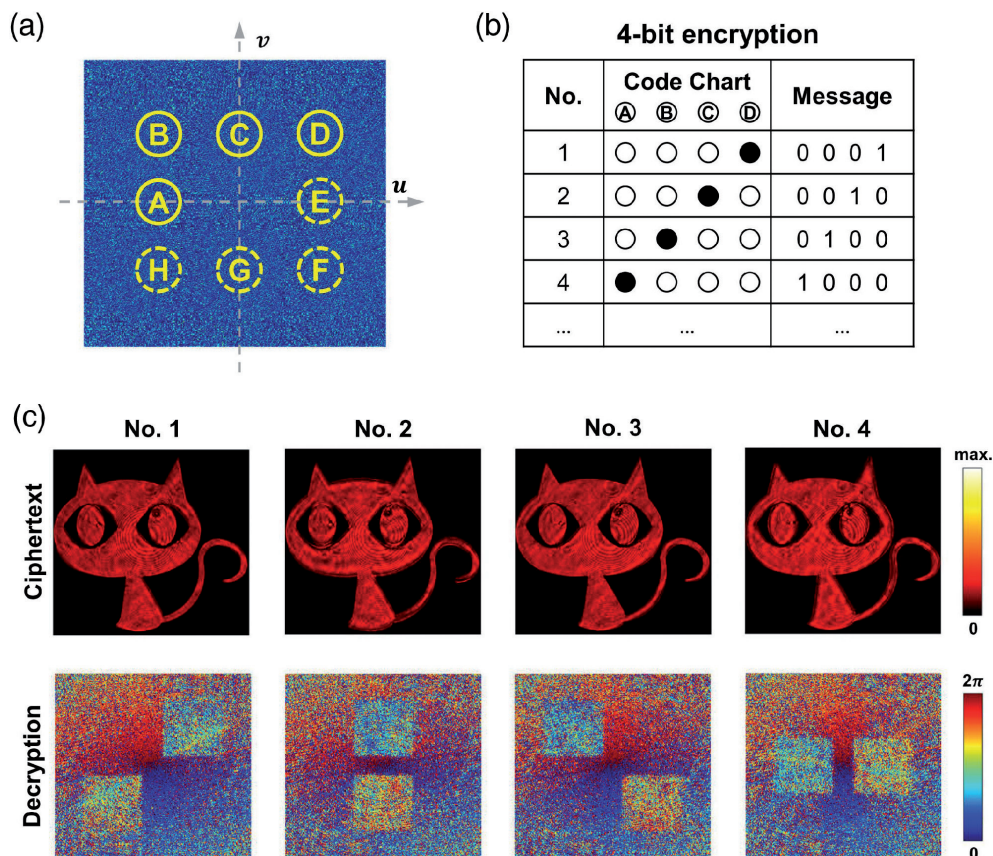


Fig. 23. Illustration of spatial frequency multiplexing encryption and experimental results of 4-bit encryption [34]: (a) Spatial frequency regions (yellow circles) for multiplexing. (b) 4-bit encryption method. Specific messages may be presented according to a code table. For a code diagram, a full circle indicates phase encryption is activated, and an empty circle indicates no change in spatial frequency. (c) Experimental results of ciphertext image and corresponding decrypted results for four messages.

above [34]. In the spatial frequency domain of an image, a specific region can act as a channel, as shown by the yellow circles and capital letters A to H in Fig. 23*a*. In fact, other regions can be used as well. We select four of these regions, namely A to D , to implement 4-bit encryption, which is described in Fig. 23*b*.

For example, if region D has phase modulation and the others do not, the encrypted message will be "0001". Similarly, other messages such as "1000", "0100" and "0010" can be encrypted with different regions, and additional combinations can be created. The experiment results are shown in Fig. 23*c* [34]. It can be found that the four ciphertext images are similar and it is difficult to distinguish which message was encrypted. Even by observing the intensity and phase of the spatial frequency, the message is also impossible to identify. However, the message can be obtained by extracting the phase difference and then accessing the code table. It should be noted that the rectangular areas in the deciphered phase difference pattern shown in Fig. 23*c*, correspond to the entire MS area. The pattern will also represent conjugate rectangular shapes relative to the encrypted region as a result of the Fourier transform operation applied to the encrypted image. We selected several regions of lower spatial frequencies around the center of the spatial frequency region to demonstrate the proposed optical encryption method. However, higher spatial frequencies can also be used to increase information capacity.

7.6. FEATURES AND PROSPECTS OF ENCRYPTION AT SPATIAL FREQUENCIES

In most optical encryption methods with MS, information is encrypted in metasurface hardware devices, which, on the one hand, enhances security, and on the other hand,

limits the delivery and processing of information. On the contrary, here the information is encrypted in optical images programmatically through the MS, rather than encrypted in the MS themselves. This avoids the physical delivery of MS, thereby facilitating transportation and information exchange. While the security in traditional encryption methods, in which information can be effectively hidden in the MS, is becoming higher and higher, the security in the proposed method can also be achieved by exploiting complex spatial frequency distributions and using the original optical images as keys. Since both security and throughput are important for encryption, multiplexing different encryption channels and using flexible encoding rules is a promising strategy to increase the throughput of the proposed method. Since MSs directly modulate the spatial frequencies of optical images, other adaptation degrees of freedom for light fields and the possibility of parallel processing can be further explored to improve security and information encryption capabilities. In addition, the decryption process of the proposed method is suitable for practical applications because it is robust to the degradation of ciphertext image quality even when the ciphertext image is corrupted in practice. In addition, the security analysis shows that the encrypted information cannot be correctly extracted if incorrect images are used as keys, which guarantees the security of the proposed method (see Appendix 1, Section 8 in [34]). The MSs operate as analog optical processors in the proposed method, which can promote ultra-fast information encryption with low power consumption and high throughput, a good complement to the digital analog.

Thus, in [34], an optical encryption method using the spatial frequencies of light field patterns was proposed and experimentally demonstrated. The intensity and phase distributions of spatial frequencies were encoded by MS for optical images. The results show that the image of the ciphertext is almost identical to the original one and no information can be identified directly, while decryption can be carried out using the Fourier transform and further operations. Additionally, the abundance of spatial frequencies in optical images is shown to provide a promising platform for flexible encoding rules, increasing the number of information channels and subsequently the encryption capabilities. This method can pave the way for the development of new methods for encrypting information, facilitating research in the field of storage, transmission, display of information, etc.

8. CONCLUSION

Currently, meta-optics has realized many optical applications that can control the phase, frequency, polarization, amplitude and propagation direction of light. But do we always need volumetric 3D metamaterials to achieve useful functionality? No. The force of interaction of electromagnetic waves with a single subwavelength layer of resonators can be large and sufficient for beam control, beam focusing and similar applications with a single layer of metamaterial or MS. The complexity of fabricating bulk metamaterials has actually driven the field into fruitful activity, and the desirability of ultrathin optical components, often referred to as planar optics, is undeniable.

Microscopic image processing, quantum image processing, holographic image processing and all-optical convolutional chip

are discussed in [18]. AI-powered meta-optics demonstrates self-monitoring capabilities.

Compared with computing with electrons as the medium, photonic computing naturally has the advantages of high-dimensional information transmission and strong parallel transmission capability. Although digital technology is relatively mature, its power consumption is high and its speed is slow. All-optical computing is an alternative scheme. Early research into bulk metamaterials and exotic properties has been supplanted by work on thin metasurfaces, ripe for commercialization, as outlined in the 2023 issue “Metasurfaces Go Mainstream” [8].

AI technology applied in meta-optics will help design complex optical structures and quickly obtain an optimal solution to the problem to meet the needs of new functions. Currently, the volume of data processing is increasing sharply, and photons carrying multi-dimensional information can effectively expand the throughput of information operations. Artificial intelligence and metasurface optics in synergy will help the research and development of advanced optical chips [1], which will promote the implementation of the next generation of optical devices and systems, and take human civilization to a higher level in the future.

REFERENCES

1. Chen Mu Ku, Liu Xiaoyuan, Sun Yanni, and Tsai Din Ping. Artificial Intelligence in Meta-optics. *Chemical Reviews*, 2022, 122(19):15356-15413.
2. Su Vin-Cent, Chu Cheng Hung, Sun Greg, and Tsai Din Ping. Advances in optical metasurfaces: fabrication and applications. *Opt. Express*, 2018, 26(10):13148-13182.
3. Qiu Cheng-Wei, Zhang Tan, Hu Guangwei, and Kivshar Yuri. Quo Vadis, Metasurfaces? *Nano Letters*, 2021, 21(13):5461-5474.

4. Liu W, Li Z, Cheng H, Chen S. Dielectric Resonance-Based Optical Metasurfaces: From Fundamentals to Applications. *iScience*, 2020, 23(12). Article No. 101868.
5. Chen Mu Ku, Leng Borui, Fan Yubin, Yao Jin, Liang Yao, Zhang Jingcheng, Liu Xiaoyuan, Sun Linshan, and Tsai Din Ping. High dimensional optical meta-devices: classical to quantum. *Proc. SPIE*, 2022, 12231. ODS 2022: Industrial Optical Devices and Systems, Article No. 1223101.
6. Abdelraouf Omar AM, Wang Ziyu, Liu Hailong, Dong Zhaogang, Wang Qian, Ye Ming, Wang Xiao Renshaw, Wang Qi Jie, Liu Hong. Recent Advances in Tunable Metasurfaces: Materials, Design, and Applications. *ACS Nano*, 2022, 16(9):13339-13369.
7. Padilla WJ, Averitt RD. Imaging with metamaterials. *Nature Reviews Phys.*, 2022, 4(2):85-100.
8. Editorials. Metasurfaces go mainstream. *Nature Photonics*. 2023, 17(1):1. DOI: 10.1038/s41566-022-01137-1.
9. Alexander A. Potapov. Computational Dielectric Metasurfaces in Photonic Topological Devices for Multidimensional Signal Processing. *RENSIT: Radioelectronics. Nanosystems. Information Technologies*, 2024, 16(1):11-30e. DOI: 10.17725/rensit.2024.16.011.
10. Wan Lei, Pan Danping, Yang Shuaifeng, Zhang Wei, Potapov Alexander A., Wu Xia, Liu Weiping, Feng Tianhua, and Li Zhaohui. Optical analog computing of spatial differentiation and edge detection with dielectric metasurfaces. *Optics Letters*, 2020, 45(7):2070-2073.
11. Pan Danping, Wan Lei, Potapov Alexander A., and Feng Tianhua. Performing Spatial Differentiation and Edge Detection with Dielectric metasurfaces. *QELS_ Fundamental Science "OSA Technical Digest Conf. on Lasers and Electro-Optics (CLEO)*. Washington: Optical Society of America, 2020. Paper FW4B.2.pdf, 2 pp. (From the session "Inverse Design and Computation (FW4B)").
12. Feng Tianhua, Potapov Alexander A., Liang Zixian, and Xu Yi. Huygens Metasurfaces Based on Congener Dipole Excitations. *Physical Review Applied*, 2020, 13, 6 p. Article No. 021002.
13. Tianhua Feng, Shuaifeng Yang, Ning Lai, Weilian Chen, Danping Pan, Wei Zhang, Potapov Alexander A., Zixian Liang, and Yi Xu. Manipulating light scattering by nanoparticles with magnetoelectric coupling. *Phys. Rev. B.*, 2020, 102, 7p. Article No. 205428.
14. Wan Lei, Pan Danping, Ouyang Min, Zhang Wei, Potapov Alexander A., Liu Weiping, Liang Zixian, Feng Tianhua, Li Zhaohui. Laplace metasurfaces for optical analog computing based on quasi-bound states in the continuum. *Photonics Research*, 2021, 9(9):1758-1766.
15. Wan Lei, Pan Danping, Feng Tianhua, Liu Weiping, Potapov A.A. A review of dielectric optical metasurfaces for spatial differentiation and edge detection. *Frontiers of Optoelectronics*, 2021, 14(2):187–200.
16. Shuaifeng Yang, Lei Wan, Fugen Wang, Alexander A. Potapov, and Tianhua Feng. Strong optomechanical coupling in chain-like waveguides of silicon nanoparticles with quasi-bound states in the continuum. *Opt. Lett.*, 2021, 46(18):4466-4469.
17. Wang Fugen, Yuan Jin, Yang Shuaifeng, Potapov Alexander A., Zhang Xin, Liang Zixian, and Feng Tianhua. Compact ring resonators of silicon nanorods for strong optomechanical interaction.

- Nanoscale*, 2023, 15(7), doi: 10.1039/D2NR06449A.
18. Xu Dingyu, Wen Shuangchun, and Luo Hailu. Metasurface-Based Optical Analog Computing: From Fundamentals to Applications. *Advanced Devices & Instrumentation*, 2022, Vol.2022. Article No. 0002;- doi: 10.34133/adi.0002.
 19. Hail Claudio U, Foley Morgan, Sokhoyan Ruzan, Michaeli Lior, Atwater Harry A. High quality factor metasurfaces for two-dimensional wavefront manipulation. <https://arxiv.org/abs/2212.05647> (12 декабря 2022). 19 p.
 20. Li Lianlin, Zhao Hanting, Liu Che, Li Long, and Cui Tie Jun. Intelligent metasurfaces: control, communication and computing. *eLight*, 2022, 2(7); doi: 10.1186/s43593-022-00013-3.
 21. Zhao Xiaoguang, Sun Zhenci, Zhang Lingyun, Wang Zilun, Xie Rongbo, Zhao Jiahao, You Rui, and You Zheng. Review on Metasurfaces: An Alternative Approach to Advanced Devices and Instruments. *Advanced Devices & Instrumentation*, 2022, vol. 2022. Article No. 9765089; doi: 10.34133/2022/9765089.
 22. Badloe T, Lee S, Rho J. Computation at the speed of light: metamaterials for all-optical calculations and neural networks. *Advanced Photonics*, 2022, 4(6), 21 p. Article No. 064002; doi: 10.1117/1.AP.4.6.064002.
 23. Saifullah Yasir, He Yejun, Boag Amir, Yang Guo-Min, and Xu Feng. Recent Progress in Reconfigurable and Intelligent Metasurfaces: A Comprehensive Review of Tuning Mechanisms, Hardware Designs, and Applications. *Advanced Science*, 2022, 9(33), 35 p. Article No. 2203747.
 24. Johnson William B, Lindenstrauss Joram. Extensions of Lipschitz mappings into a Hilbert space. *Proc. Conf. in Modern Analysis and Probability* (New Haven, Conn., June 8-11, 1982), P. 189-206, Contemporary Mathematics, V. 26, Amer. Math. Soc., Providence, RI, 1984.
 25. Li Lianlin, Ruan Hengxin, Liu Che, Li Ying, Shuang Ya, Alù Andrea, Qiu Cheng-Wei, and Cui Tie Jun. Machine-learning reprogrammable metasurface imager. *Nature Communications*, 2019, 10. Article No.1082.
 26. Zheng Peixia, Dai Qi, Li Zile, Ye Zhiyuan, Xiong Jun, Liu Hong-Chao, Zheng Guoxing, Zhang Shuang. Metasurface-based key for computational imaging encryption. *Science Advances*, 2021, 7(21). DOI: 10.1126/sciadv.abg0363.
 27. Xiao Qiang, Ma Qian, Yan Tao, Wu Liang Wei, Liu Che, Wang Zheng Xing, Wan Xiang, Cheng Qiang, Cui Tie Jun. Orbital-Angular-Momentum-Encrypted Holography Based on Coding Information Metasurface. *Advanced Optical Materials*, 2021, 9(11), doi: 10.1002/adom.202002155.
 28. Wu Liang Wei, Xiao Qiang, Gou Yue, Wu Rui Yuan, Xu Peng, Qing Ye Ming, Wang Zheng Xing, Bao Lei, Ma Hui Feng, Cui Tie Jun. Electromagnetic Diffusion and Encryption Holography Integration Based on Reflection-Transmission Reconfigurable Digital Coding Metasurface. *Advanced Optical Materials*, 2022, 10(10), doi: 10.1002/adom.202102657.
 29. Xuqian Jiang, Ye Fujun, Tan Hongrui, Luo Sisi, Cui Haoyang, and Chen Lei. Digital Programmable Metasurface with Element-Independent Visible-Light Sensing. *Electronics*, 2023, 12(1). 9 p., doi: 10.3390/electronics12010241.
 30. Cui Tie Jun, Qi Mei Qing, Wan Xiang, Zhao Jie, Cheng Qiang. Coding

- metamaterials, digital metamaterials and programmable metamaterials. *Light: Science & Applications*, 2014, 3(e218), 9 p. doi: 10.1038/lisa.2014.99.
31. Ma Qian, Gao Wei, Xiao, Qiang, Ding Lingsong, Gao Tianyi, Zhou Yajun, Gao Xinxin, Yan Tao, Liu Che, Gu Ze, Kong Xianghong, Abbasi Qammer H., Li Lianlin, Qiu Cheng-Wei, Li Yuanqing, and Cui Tie Jun. Directly wireless communication of human minds via non-invasive brain-computer-metasurface platform. *eLight*, 2022, 2(1). doi: 10.1186/s43593-022-00019-x.
32. Wang Hai Lin, Ma Hui Feng, Cui Tie Jun. A Polarization-Modulated Information Metasurface for Encryption Wireless Communications. *Advanced Science*, 2022, 9(34). 9 p., doi: 10.1002/advs.202204333.
33. Wang Hai Lin, Zhang Yan Kai, Zhang Tai Yi, Ma Hui Feng, and Cui Tie Jun. Broadband and Programmable Amplitude-Phase-Joint-Coding Information Metasurface. *ACS Applied Materials & Interfaces*, 2022, 14(25):29431-29440.
34. Ouyang Min, Yu Haoyang, Pan Danping, Wan Lei, Zhang Cheng, Gao Shecheng, Feng Tianhua, and Li Zhaohui. Optical encryption in spatial frequencies of light fields with metasurfaces. *Optica*, 2022, 9(9):1022-1028.